Electronic Supporting Information for

Columnar liquid crystalline triphenylene-bis(dithiolene)nickel complexes. Soft photothermal materials

Silvia Cobos,[a] Gregorio García,[a] César L. Folcia,[b] Josu Ortega,[b] Jesús Etxebarria,[b] Gabriel López- Peña,[c] Dirk H. Ortgies,[d,e] Emma Martín Rodríguez,[c,e] and Silverio Coco.*[a]*

[a] IU CINQUIMA/Química Inorgánica, Facultad de Ciencias, Universidad de Valladolid, 47071 Valladolid, Castilla y León, Spain.

[b] Department of Physics, University of the Basque Country, UPV/EHU, 48080 Bilbao, Spain.

[c] Departamento de Física Aplicada, Universidad Autónoma de Madrid, C/ Francisco Tomás y Valiente 7, 28049, Madrid, Spain.

[d] Departamento de Física de Materiales, Universidad Autónoma de Madrid, C/ Francisco Tomás y Valiente 7, 28049, Madrid, Spain.

[e] nanomaterials for BioImaging Group, Instituto Ramón y Cajal de Investigación Sanitaria IRYCIS, Ctra. de Colmenar km 9, 300, 28034, Madrid, Spain.

Table of Contents

Experimental Section

General Considerations. General procedures are as reported before. Elemental analyses were performed by the "Servicio de análisis elemental, CACTI, Universidad de Vigo". IR spectra were recorded on a Perkin-Elmer Frontier spectrometer coupled to a Pike GladiATR-210 accessory. NMR spectra were recorded on Varian 500 instruments in $CDCl_3$. MALDI-TOF MS was performed using a Bruker Daltonics autoflex speed instrument equipped with nitrogen laser (340 nm). Positive-ion mode spectra were recorded using the reflective mode. The accelerating voltage was 19 kV. The analytical sample was obtained by mixing the dichloromethane or tetrahydrofurane solution of the sample (1 mg/mL) and a solution of the matrix in the same solvent (DCTB, 10 mg/mL) in a 1/5 (vol/vol) ratio. The prepared solution of the sample and the matrix (0.5 μL) was loaded on the MALDI plate and allowed to dry at 23ºC before the plate was inserted into the vacuum chamber of the MALDI instrument. UV/Vis spectra were recorded on Shimadzu UV-2550 or UV-1603 spectrophotometers. Luminescence spectra were recorded with a Perkin-Elmer LS-55 spectrometer in CH_2Cl_2. Photoluminescence quantum yield (QY) was measured with a FLS980 fluorescence spectrometer (Edinburgh Instruments) equipped with an integrating sphere. Fluorescence decays in dichloromethane, at room temperature. Lifetimes were obtained with the Time Correlated Single Photon Counting (TCSPC) and MCP-PMT counter module (TCC2) of the FLS980 spectrometer. Fluorescence decays were analyzed with the method of non-linear least squares iterative deconvolution ant the quality of the fits was judged by the values of the reduced Chi-square (c2) and the autocorrelation function of the residuals using the FAST (Advanced Fluorescence Lifetime Analysis Software) program provided by the equipment. Reconvolution Fit Analysis was used to fit a measured sample decay (red line in Figures) taking into account the IRF Instrument Response Function (black line in Figures). IRF was determined by using Ludox (a scatterer) instead of the sample.

Microscopy studies were carried out on a Leica DMRB microscope equipped with a Mettler FP82HT hot stage and a Mettler FP90 central processor, at a heating rate of 10 °C min^{-1}. DSC was performed using a DSC Q20 from TA Instruments with samples (2−5 mg) sealed in aluminum pans and a scanning rate of 10 °C/min under a nitrogen atmosphere.

Thermogravimetric analyses (TGA) were carried out with a thermogravimetric analyser model TGA/SDTA 861. The samples were heated from 50°C to 1000°C at 10 °C/min under N_2 atmosphere.

For the photothermal studies, the solid complex was placed inside the beam of a Lumics fiber-coupled laser diode in a transparent 0.5 mL microcentrifuge tube at a distance allowing the beam to open up to cover the material. A thermal camara (FLIR E-54) was located to the side of the sample and focused on the tube. After thermal equilibration the power output of the diode was adjusted to three power densities (0.024, 0.060 and 0.098 W/cm2) and turned on for 4 minutes, then switched off while the temperature was recorded during heating and cooling. The 690 nm laser diode used for the control experiment is a custom-build model from Lasing, S.A., Spain with a DG-31 diode controller.

Synthesis. Literature methods were used for the synthesis of 2-hydroxy-3,6,7,10,11-pentakis(dodecyloxy)triphenylene.[1]

Only examples are described, as the syntheses were similar for the rest of the complexes. Yields, IR, and analytical data are given for all the complexes.

Preparation of 2-(n-bromoalkoxy)-3,6,7,10,11-pentakis(dodecyloxy)triphenylene.

To a solution of 2-hydroxy- 3,6,7,10,11-pentakis(dodecyloxy)triphenylene (0.60 mmol) in dry butanone (15 mL) under nitrogen, 1,n-dibromoalkane (9.00 mmol) and K_2CO_3 (0.83 g, 6.03 mmol) were added. The mixture was refluxed for 22 h and then the solvent was evaporated. To the obtained residue, water (10 mL) was added and the mixture was extracted with dichloromethane (3 x 10 mL).

The organic layer was separated, dried over MgSO$_4$ and filtered. The solvent was removed on a rotary evaporator, and the residue was recrystallized from acetone, yielding the compound as a cream solid.

2-(2-bromoethoxy)-3,6,7,10,11-pentakis(dodecyloxy)triphenylene. Yield: 0.54 g; 70 %. ^{1}H RMN (CDCl$_3$): δ 7.93 (s, 1H, TriPh), 7.84-7.82 (m, 5H, TriPh), 4.25 (m, 10H, TriPh-O-CH$_2$), 3.76 (t, 4H, CH$_2$Br, J = 6.7 Hz), 1.96-1.90 (m, 10H, O-CH$_2$-*CH$_2$*), 1.59-1.26 (m, 90H, CH$_2$), 0.88 (t, 15H, CH$_3$, J = 6.4 Hz).

2-(6-bromohexyloxy)-3,6,7,10,11-pentakis(dodecyloxy)triphenylene. Yield: 0.73 g; 92 %. ^{1}H RMN (CDCl$_3$): δ 7.83 (s, 6H, TriPh), 4.24 (m, 12H, TriPh-O-CH$_2$), 3.45 (t, 2H, CH$_2$Br, J = 6.8 Hz), 1.96-1.91 (m, 12H, O-CH$_2$-*CH$_2$*), 1.60-1.24 (m, 96H, CH$_2$), 0.88 (t, 15H, CH$_3$, J = 7.0 Hz).

2-(10-bromodecyloxy)-3,6,7,10,11-pentakis(dodecyloxy)triphenylene. Yield: 0.72 g; 89 %. ^{1}H RMN (CDCl$_3$): δ 7.83 (s, 6H, TriPh), 4.22 (t, 12H, TriPh-O-CH$_2$, J = 6.5 Hz), 3.39 (t, 2H, CH$_2$Br, J = 6.5 Hz), 1.96-1.90 (m, 12H, O-CH$_2$-*CH$_2$*), 1.88-1.82 (m, 2H, Br-CH$_2$-*CH$_2$*), 1.59-1.26 (m, 102H, CH$_2$), 0.87 (t, 15H, CH$_3$, J = 7.0 Hz).

Preparation of benzil precursors (1-3)

To a solution of 1,2-bis(4-hydroxyphenyl)ethane-1,2-dione (0.07 mmol) in dry butanone (25 mL) under nitrogen, 2-(n-bromoalkoxy)-3,6,7,10,11-pentakis(dodecyloxy)triphenylene (0.31 mmol) and K$_2$CO$_3$ (0.09 g, 0.64 mmol) were added. The mixture was refluxed for 24 h and then the solvent was evaporated. To the obtained residue, water (15 mL) was added and the mixture was extracted with dichloromethane (4 x 15 mL). The organic layer was separated, dried over MgSO$_4$ and filtered. The solvent was removed on a rotary evaporator. The product was purified by column chromatography (silica gel, dichloromethane/hexane 4:1 v/v as eluent). The solvent was evaporated to obtain a yellow solid.

1,2-bis(4-(2-((3,6,7,10,11-pentakis(dodecyloxy)triphenylen-2-yl)oxy)ethoxy)phenyl)ethane-1,2-dione (1). Yield: 0.11 g; 53 %. ^{1}H RMN (CDCl$_3$): δ 7.98 (d, 4H, ArH^A, AA' part of AA'XX' spin system, $N_{A,X} = J_{AX} + J_{AX'} = 9$ Hz, $J_{AA'} \approx J_{XX'}$), 7.96 (s, 2H, TriPh), 7.87-7.80 (m, 10H, TriPh), 7.08 (d, 4H, ArH^X, XX' part of AA'XX' spin system, $N_{A,X} = J_{AX} + J_{AX'} = 9$ Hz, $J_{AA'} \approx J_{XX'}$), 4.61 (t, 4H, OCH$_2$, J = 4.77 Hz), 4.52 (t, 4H, OCH$_2$, J = 4.77 Hz), 4.22 (m 20H, TriPh-O-CH$_2$), 1.96-1.26 (m, 200H, CH$_2$), 0.87 (m, 30H, CH$_3$). ^{13}C{^{1}H}NMR (CDCl$_3$): δ 193.17 (OC-CO), 164.04 (O-*CPh*), 149.28, 149.21, 149.15, 149.09, 148.99, 148.03 (O-*CTriPh*), 132.42 (*CPh*), 126.63 (HA-*CPh*), 124.76, 123.95, 123.58, 123.51, 123.35 (*CTriPh*), 114.92 (HX-*CPh*), 109.73, 107.59, 107.28, 107.22, (H-*CTriPh*), 69.83, 69.78, 69.68, 69.54, 68.73 (TriPh-*OCH$_2$*), 67.35 (Ph-*OCH$_2$*), 31.94, 31.92, 29.74, 29.72, 29.70, 29.69, 29.66, 29.64, 29.56, 29.54, 29.50, 29.48, 29.42, 29.39, 29.36, 26.22, 26.18, 22.70 (*CH$_2$*), 14.12 (*CH$_3$*). Elemental analysis for C$_{174}$H$_{278}$O$_{16}$ (%): calculated C, 79.58; H, 10.67; found C, 79.64; H, 10.82. MS (MALDI-TOF): m/z calc. for [C$_{174}$H$_{278}$O$_{16}$ (M$^+$)]: 2624.0934; found 2624.04889. IR: ν(C=O): 1660 cm^{-1}.

1,2-bis(4-((6-((3,6,7,10,11-pentakis(dodecyloxy)triphenylen-2-yl)oxy)hexyl)oxy)phenyl) ethane-1,2-dione (2). Yield: 0.13 g; 73 %. ^{1}H RMN (CDCl$_3$): δ 7.93 (d, 4H, ArH^A, AA' part of AA'XX' spin system, $N_{A,X} = J_{AX} + J_{AX'} = 8.95$ Hz, $J_{AA'} \approx J_{XX'}$), 7.83 (s, 12H, TriPh), 6.95 (d, 4H, ArH^X, XX' part of AA'XX' spin system, $N_{A,X} = J_{AX} + J_{AX'} = 8.95$ Hz, $J_{AA'} \approx J_{XX'}$), 4.22 (m 24H, TriPh-O-CH$_2$), 4.06 (t, 4H, ArOCH$_2$, J = 4.06 Hz), 1.98-1.26 (m, 220H, CH$_2$), 0.87 (m, 30H, CH$_3$). ^{13}C{^{1}H}NMR (CDCl$_3$): δ 193.42 (OC-CO), 164.41 (O-*CPh*), 149.05, 149.03, 149.00, 148.97, 148.95, 148.83 (O-*CTriPh*), 132.35 (*CPh*), 126.15 (HA-*CPh*), 123.72, 123.68, 123.65, 123.58, 123.56 (*CTriPh*), 114.66 (HX-*CPh*), 107.53, 107.47, 107.42, 107.37, 107.23 (H-*CTriPh*), 69.82, 69.75, 69.72, 69.70, 69.60, 69.52 (TriPh-*OCH$_2$*), 68.33 (Ph-*OCH$_2$*), 31.91, 29.73, 29.70, 29.68, 29.66, 29.65, 29.55, 29.52, 29.49, 29.46, 29.43, 29.38, 29.36, 29.09, 26.21, 26.20, 26.02, 25.89, 22.69, 22.67 (*CH$_2$*), 14.10 (*CH$_3$*). Elemental analysis for C$_{182}$H$_{294}$O$_{16}$ (%): calculated C, 79.83; H, 10.82; found C, 79.92; H,

10.88. MS (MALDI-TOF): m/z calc. for [$C_{182}H_{294}O_{16}$ (M$^+$)]: 2736.2186; found 2736.2224. IR: ν(C=O): 1668 cm^{-1}.

1,2-bis(4-((10-((3,6,7,10,11-pentakis(dodecyloxy)triphenylen-2-yl)oxy)decyl)oxy)phenyl) ethylen-1,2-dione (3). Yield: 0.11 g; 53 %. ^{1}H RMN (CDCl$_3$): δ 7.92 (d, 4H, ArH^A, AA' part of AA'XX' spin system, $N_{A,X} = J_{AX} + J_{AX'} = 8.93$ Hz, $J_{AA'} \approx J_{XX'}$), 7.83 (s, 12H, TriPh), 6.93 (d, 4H, ArH^X, XX' part of AA'XX' spin system, $N_{A,X} = J_{AX} + J_{AX'} = 8.93$ Hz, $J_{AA'} \approx J_{XX'}$), 4.22 (t 24H, TriPh-O-CH$_2$, J = 6.53 Hz), 4.00 (t, 4H, ArOCH$_2$, J = 7.06 Hz), 1.96-1.26 (m, 236H, CH$_2$), 0.87 (m, 30H, CH$_3$). ^{13}C{^{1}H}NMR (CDCl$_3$): δ 193.48 (OC-CO), 164.44 (O-*CPh*), 148.96, 148.92, (O-*CTriPh*), 132.33 (*CPh*), 126.06 (HA-*CPh)*, 123.58 (*CTriPh*), 114.64 (HX-*CPh*), 107.32 (H-*CTriPh*), 69.67 (TriPh-*OCH$_2$*), 68.42 (Ph-*OCH$_2$*), 31.91, 29.71, 29.68, 29.66, 29.58, 29.52, 29.40, 29.36, 29.04, 26.19, 25.96, 22.67 (*CH$_2$*), 14.10 (*CH$_3$*). Elemental analysis for $C_{190}H_{310}O_{16}$ (%): calculated C, 80.06; H, 10.96; found C, 80.22; H, 11.02. MS (MALDI-TOF): m/z calc. for [$C_{190}H_{310}O_{16}$ (M$^+$)]: 2848.3438; found 2848.3485. IR: ν(C=O): 1668 cm^{-1}.

Preparation of bis-(dithiolene)nickel complexes (4-6).

To a solution of 4,4'-bis(2-(n-alkoxy)-3,6,7,10,11-pentakis(dodecyloxy)triphenylene)benzyl (0.056 mmol) in dry dioxane (5 mL) under nitrogen, P$_2$S$_5$ (0.14 mmol) was added. After stirring for 5 h at 130 °C, the reaction mixture was filtered at room temperature, and a solution of NiCl$_2$·6H$_2$O (0.01 mmol) in 1 ml of ethanol was added to the filtrate. The reaction mixture was heated for 2 h at 100°C under nitrogen. To the resulting mixture, water (10 mL) was added and the precipitate was filtered, washed with ethanol (3 x 10 mL) and dried under vacuum. The product was purified by column chromatography (silica gel, dichloromethane/hexane 2:1 v/v as eluent). The solvent was evaporated to obtain a dark green solid.

Bis-[1,2-di(4-((2-((3,6,7,10,11-pentakis(dodecyloxy)triphenylen-2-yl)oxy)ethoxy)phenyl) ethylen-1,2-dithiolene]nickel (4). Yield: 0.09 g; 60 %. ^{1}H RMN (CDCl$_3$): δ 7.97 (s, 2H, TriPh),

7.83 (m, 20H, TriPh), 7.38 (d, 8H, ArH^A, AA' part of AA'XX' spin system, $N_{A,X} = J_{AX} + J_{AX'} = 8.95$ Hz, $J_{AA'} \approx J_{XX'}$), 6.91 (d, 8H, ArH^X, XX' part of AA'XX' spin system, $N_{A,X} = J_{AX} + J_{AX'} = 8.95$ Hz, $J_{AA'} \approx J_{XX'}$), 4,58 (t, 8H, OCH$_2$, J = 4.06 Hz), 4.43 (t, 8H, OCH$_2$, J = 4.06 Hz) 4.21 (m, 40H, TriPh-O-CH$_2$), 1.92-1.19 (m, 400H, CH$_2$), 0.86 (m, 60H, CH$_3$). ^{13}C{^{1}H}NMR (CDCl$_3$): δ 180.38 (C*vinyl*), 159.49 (O-*CPh*), 149.19, 149.12, 149.00, 148.93, 148.19 (O-*CTriPh*), 134.67 (*CPh*), 130.39 (HA-*CPh)*, 124.59, 123.88, 123.51, 123.37 (*CTriPh*), 114.58 (HX-*CPh*), 109.56, 107.52, 107.42, 107.26, 107.10 (H-*CTriPh*), 69.77, 69.65, 69.63, 69.59, 68.86 (TriPh-*OCH$_2$*), 67.03 (Ph-*OCH$_2$*), 31.91, 29.72, 29.69, 29.67, 29.54, 29.49, 29.42, 29.36, 26.20, 22.67 (*CH$_2$*), 10.09 (*CH$_3$*). Elemental analysis for C$_{348}$H$_{556}$NiO$_{28}$S$_4$ (%): calculated C, 77.76; H, 10.43; S, 2.39; found C, 77.93; H, 10.44; S, 2.13. MS (MALDI-TOF): m/z calc. for [C$_{348}$H$_{556}$N$_i$O$_{28}$S$_4$ (M$^+$)]: 5370.0314; found 5370.0510.

Bis-[1,2-di(4-((6-((3,6,7,10,11-pentakis(dodecyloxy)triphenylen-2-yl)oxy)hexyloxy)phenyl) ethylen-1,2-dithiolene]nickel (5). Yield: 0.10 g; 67 %. ^{1}H RMN (CDCl$_3$): δ 7.83 (m, 24H, TriPh), 7.33 (d, 8H, ArH^A, AA' part of AA'XX' spin system, $N_{A,X} = J_{AX} + J_{AX'} = 8.80$ Hz, $J_{AA'} \approx J_{XX'}$), 6.80 (d, 8H, ArH^X, XX' part of AA'XX' spin system, $N_{A,X} = J_{AX} + J_{AX'} = 8.80$ Hz, $J_{AA'} \approx J_{XX'}$), 4.22 (m, 48H, TriPh-O-CH$_2$), 3.99 (t, 8H, Ph-O-CH$_2$), 1.92-1.24 (m, 442H, CH$_2$), 0.87 (m, 60H, CH$_3$). ^{13}C {^{1}H} NMR (CDCl$_3$): δ 180.39 (C*vinyl*), 159.80 (O-*CPh*), 149.00, 148.99, 148.96, 148.93, 148.86 (O-*CTriPh*), 134.23 (*CPh*), 130.32 (HA-*CPh)*, 123.68, 123.63, 123.57 (*CTriPh*), 114.27 (HX-*CPh*), 107.36, 107.26 (H-*CTriPh*), 69.77, 69.70, 69.62, 69.56, 67.95 (TriPh-*OCH$_2$*), 31.92, 29.72, 29.69, 29.67, 29.54, 29.51, 29.48, 29.46, 29.37, 29.30, 26.20, 26.09, 26.02, 22.68 (*CH$_2$*), 14.12, 14.10 (*CH$_3$*). Elemental analysis for C$_{364}$H$_{588}$NiO$_{28}$S$_4$ (%): calculated C, 78.08; H, 10.58; S, 2.29; found C, 78.37; H, 10.84; S, 2.09. MS (MALDI-TOF): m/z calc. for [C$_{364}$H$_{588}$N$_i$O$_{28}$S$_4$ (M$^+$)]: 5594.2818; found 5594.2818.

Bis-[1,2-di(4-((10-((3,6,7,10,11-pentakis(dodecyloxy)triphenylen-2-yl)oxy)decyloxy)phenyl) ethylen-1,2-dithiolene]nickel (6). Yield: 0.18 g; 60 %. ^{1}H RMN (CDCl$_3$): δ 7.83 (m, 24H, TriPh), 7.31 (d, 8H, ArH^A, AA' part of AA'XX' spin system, $N_{A,X} = J_{AX} + J_{AX'} = 8.80$ Hz, $J_{AA'} \approx J_{XX'}$), 6.77

(d, 8H, ArH^X, XX' part of AA'XX' spin system, $N_{A,X} = J_{AX} + J_{AX'} = 8.80$ Hz, $J_{AA'} \approx J_{XX'}$), 4.22 (t, 48H, TriPh-O-CH$_2$, J = 6.48 Hz), 3.93 (t, 8H, Ph-O-CH$_2$, J = 6.53 Hz), 1.92-1.53 (m, 486H, CH$_2$), 0.87 (m, 60H, CH$_3$). ^{13}C {^{1}H} NMR (CDCl$_3$): δ 180.39 (C*vinyl*), 159.83 (O-*CPh*), 148.96, 148.94 (O-*CTriPh*), 134.17 (*CPh*), 130.30 (HA-*CPh)*, 123.59 (*CTriPh*), 114.26 (HX-*CPh*), 107.42, 107.36 (H-*CTriPh*), 69.70, 68.06 (TriPh-*OCH$_2$*), 31.92, 29.72, 29.69, 29.67, 29.58, 29.54, 29.48, 29.37, 26.20, 26.09, 26.02, 22.68 (*CH$_2$*), 14.16 (*CH$_3$*). Elemental analysis for C$_{380}$H$_{620}$N$_i$O$_{28}$S$_4$ (%): calculated C, 78.37; H, 10.73; S, 2.20; found C, 78.67; H, 10.84; S, 1.88. MS (MALDI-TOF): m/z calc. for [C$_{380}$H$_{620}$N$_i$O$_{28}$S$_4$ (M$^+$)]: 5818.5322; found 5818.5014.

¹H NMR spectra (Agilent 500 in CDCl₃)

¹H NMR spectra (Agilent 500 in CDCl₃)
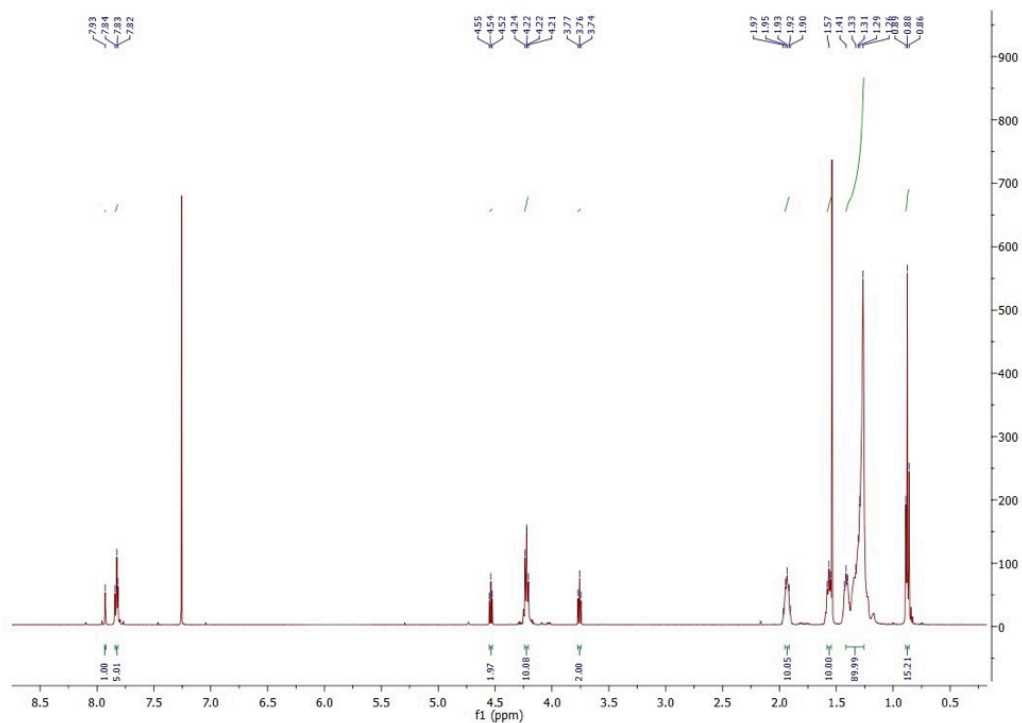
Figure S1: ¹H NMR spectrum of 2-(2-bromoethoxy)-3,6,7,10,11-
pentakis(dodecyloxy)triphenylene (**a**).
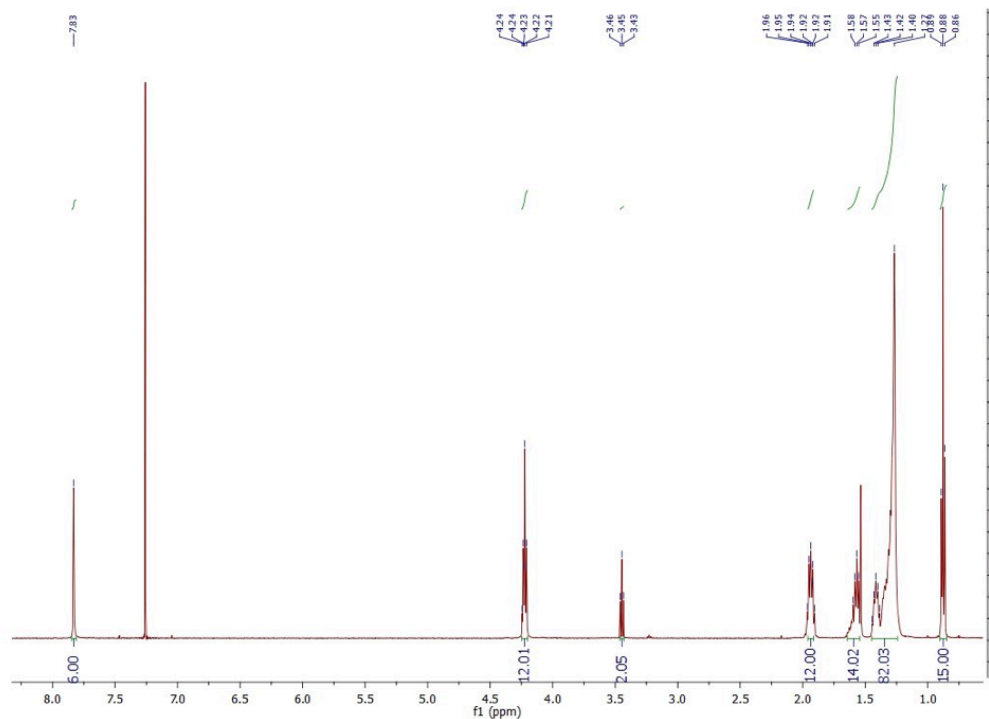
Figure S2: ¹H NMR spectrum of 2-(6-bromohexyloxy)-3,6,7,10,11-
pentakis(dodecyloxy)triphenylene (**b**)
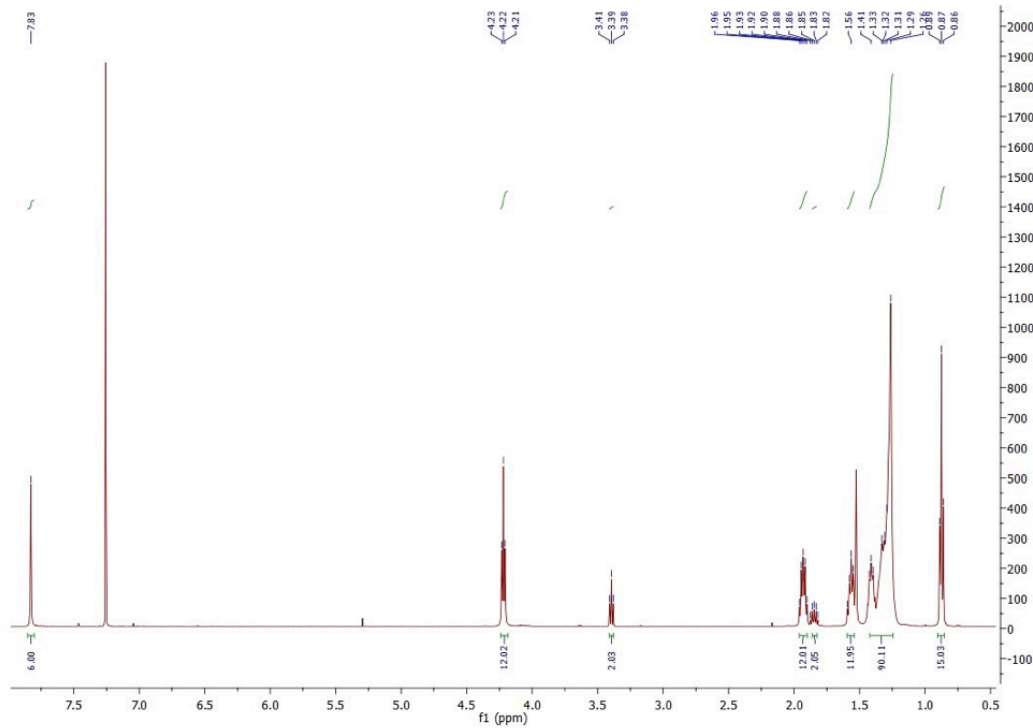
Figure S3: ^{1}H NMR spectrum of 2-(10-bromodecyloxy)-3,6,7,10,11-pentakis(dodecyloxy)triphenylene (**c**).
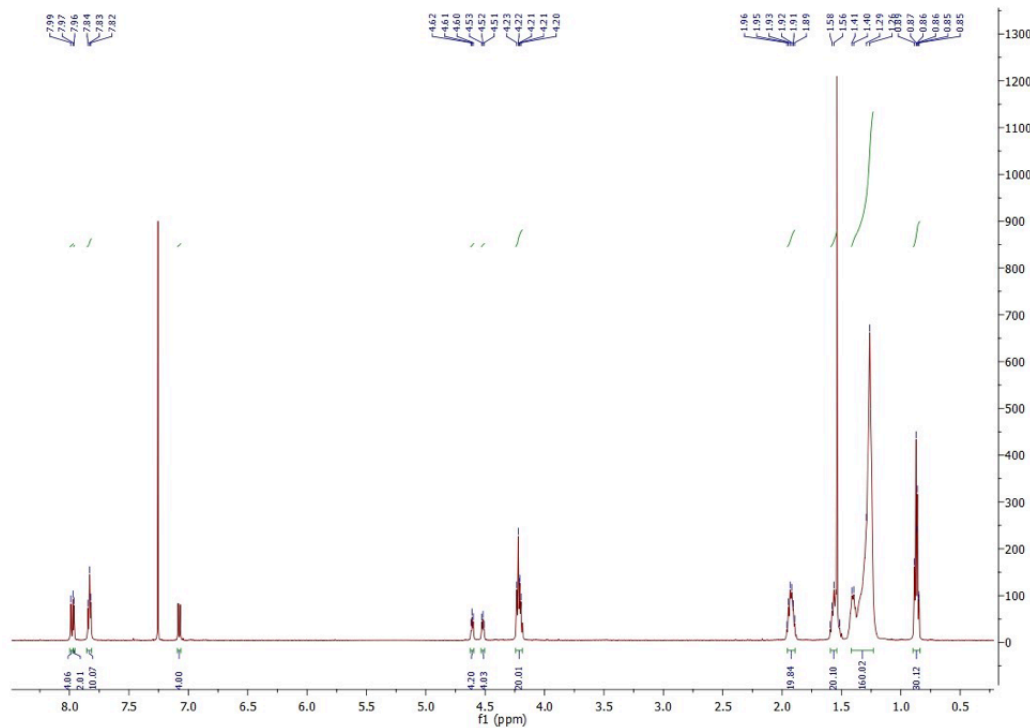
Figure S4: ^{1}H NMR spectrum of **1**.
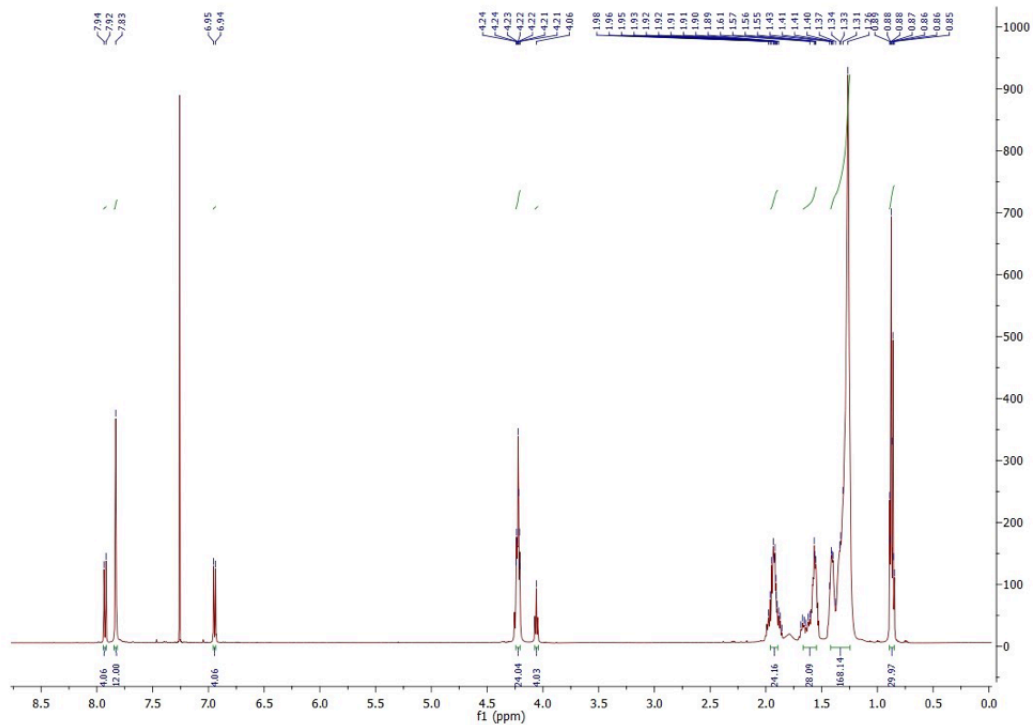
Figure S5: ^{1}H NMR spectrum of **2**.
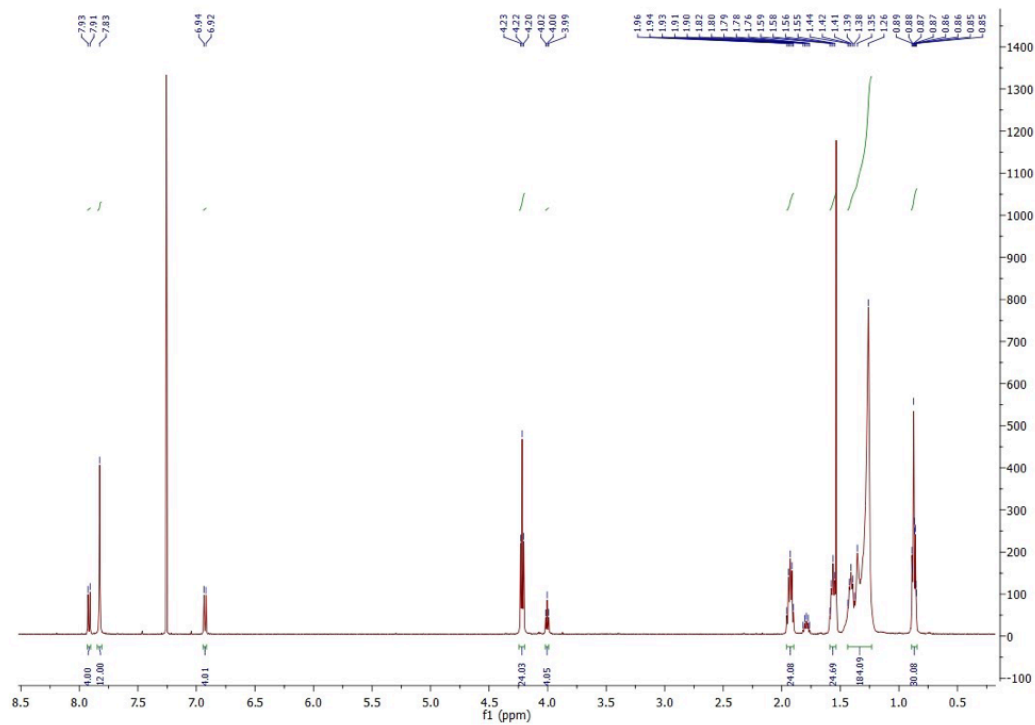
Figure S6: ^{1}H NMR spectrum of **3**.
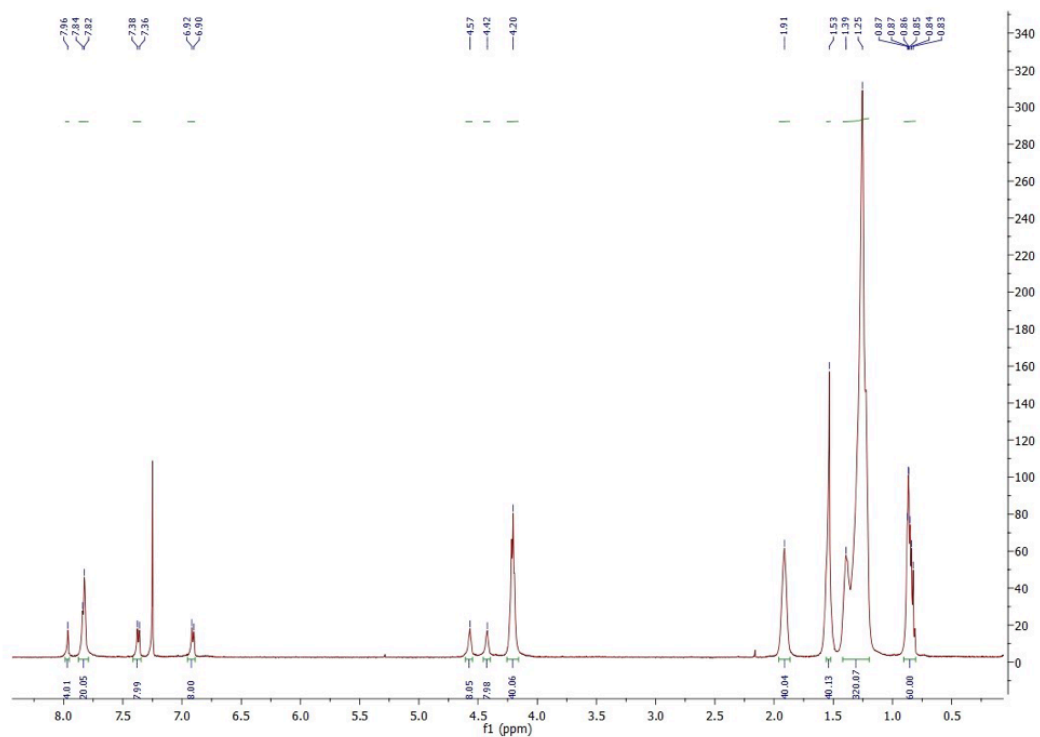
Figure S7: ^{1}H NMR spectrum of **4**.
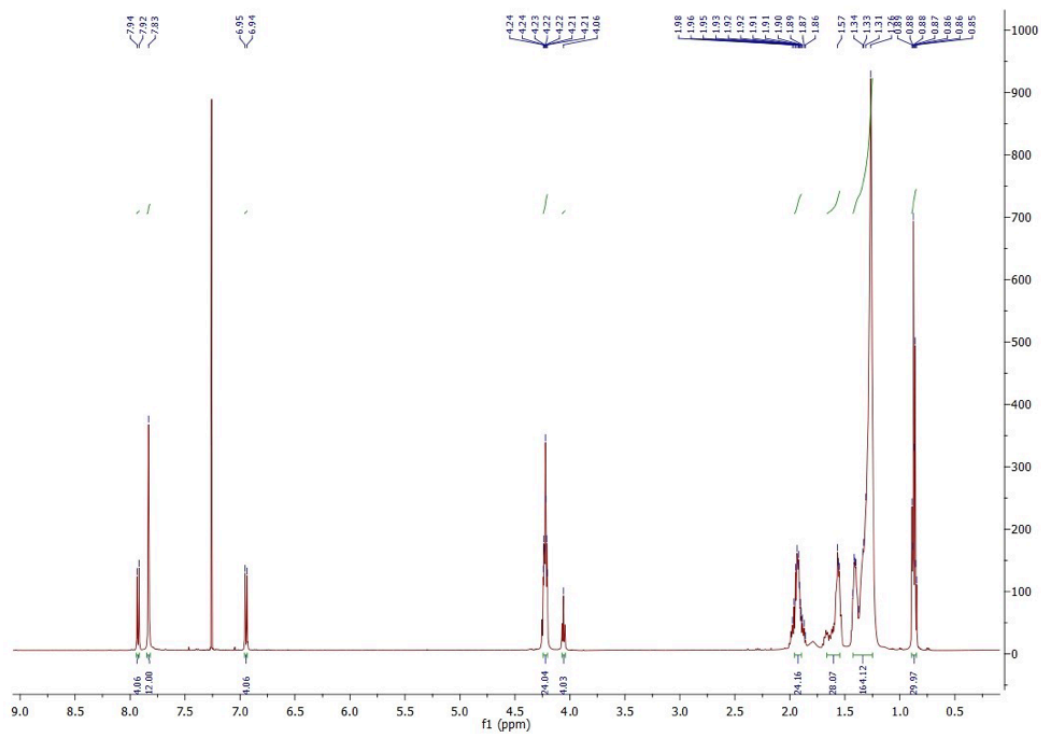
Figure S8: ^{1}H NMR spectrum of **5**.
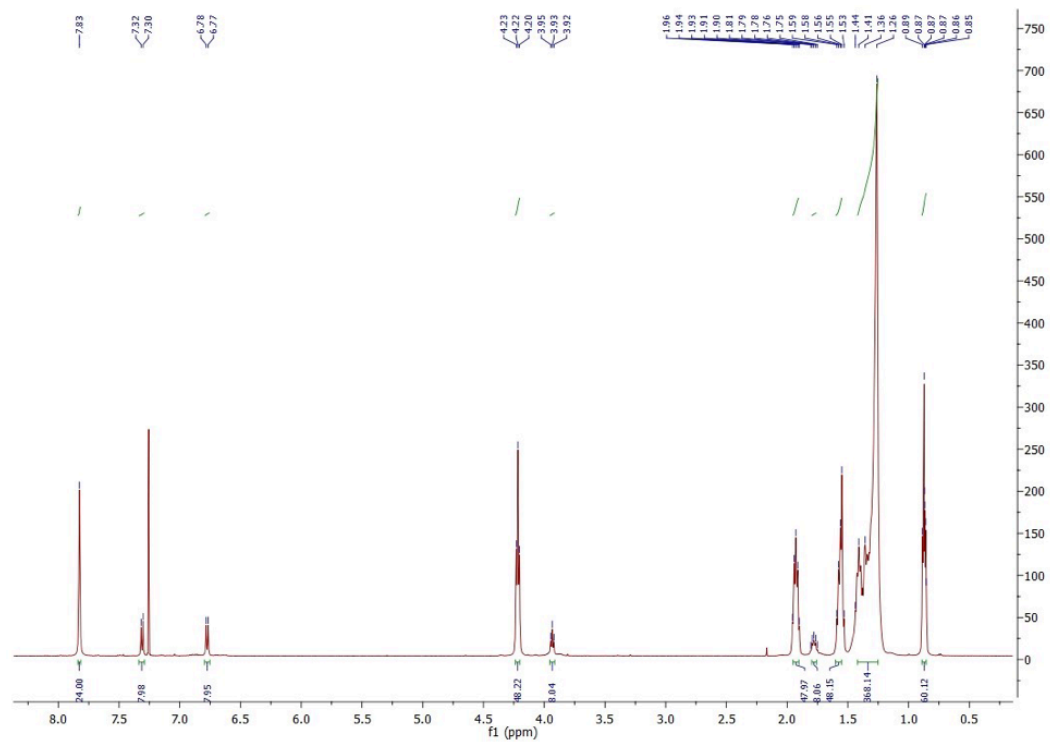
Figure S9: ^{1}H NMR spectrum of **6**.

$^{13}C\{^1H\}$ NMR spectra (Agilent 500 (126 MHz MHz) in CDCl$_3$
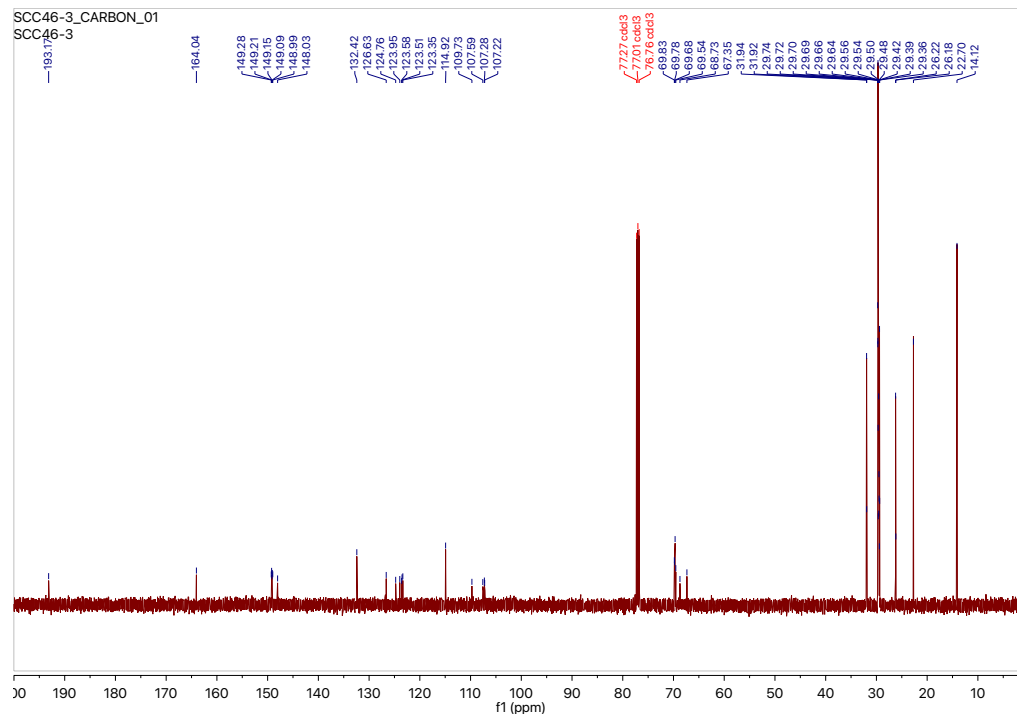
Figure S10: $^{13}C\{^1H\}$ NMR spectrum of **1**
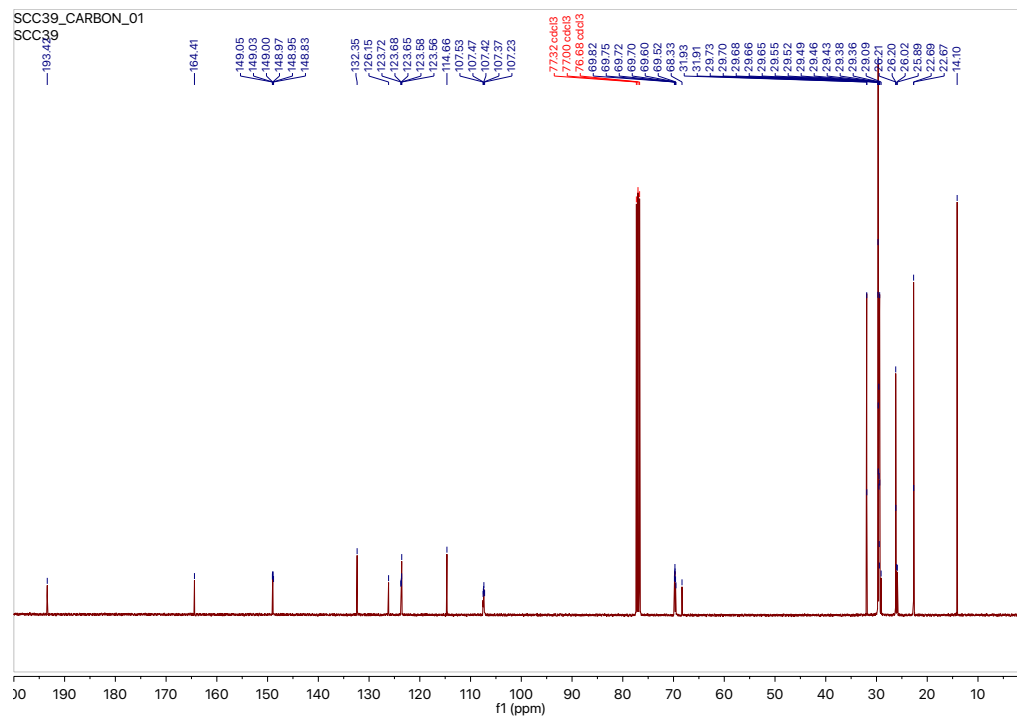
Figure S11: $^{13}C\{^1H\}$ NMR spectrum of **2**
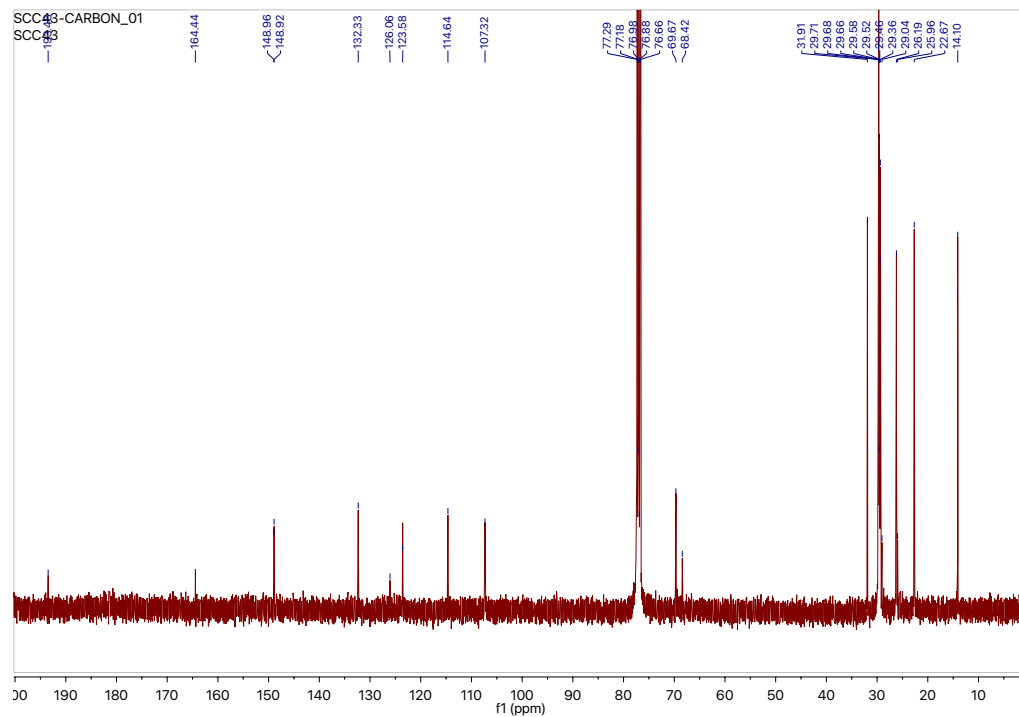
Figure S12: $^{13}C\{^1H\}$ NMR spectrum of **3**
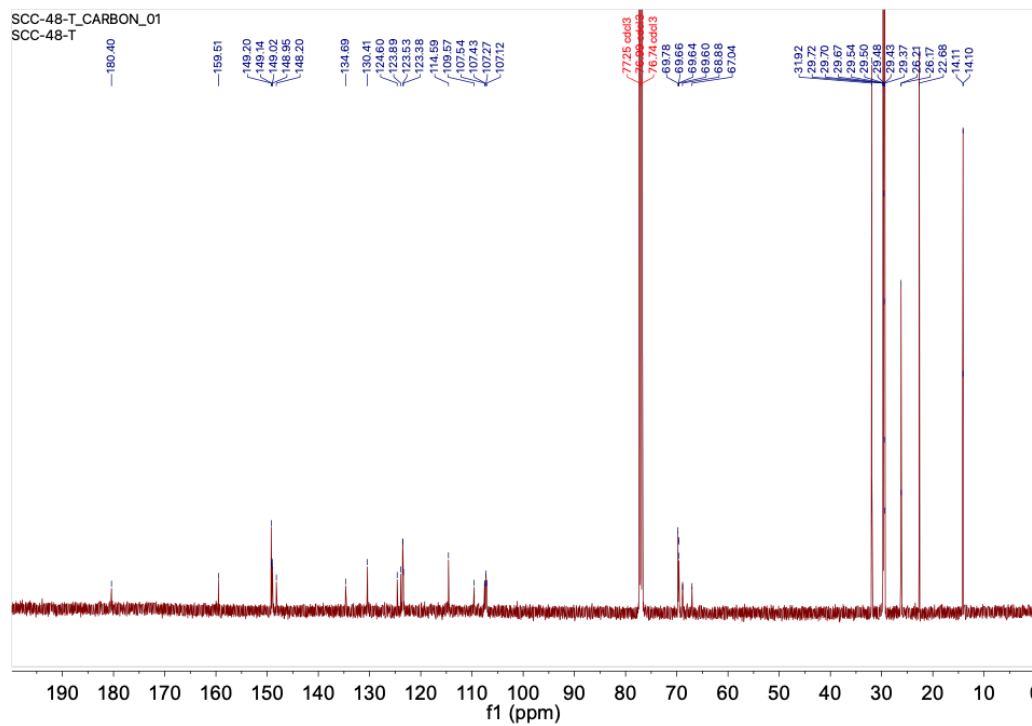
Figure S13: $^{13}C\{^1H\}$ NMR spectrum of **4**
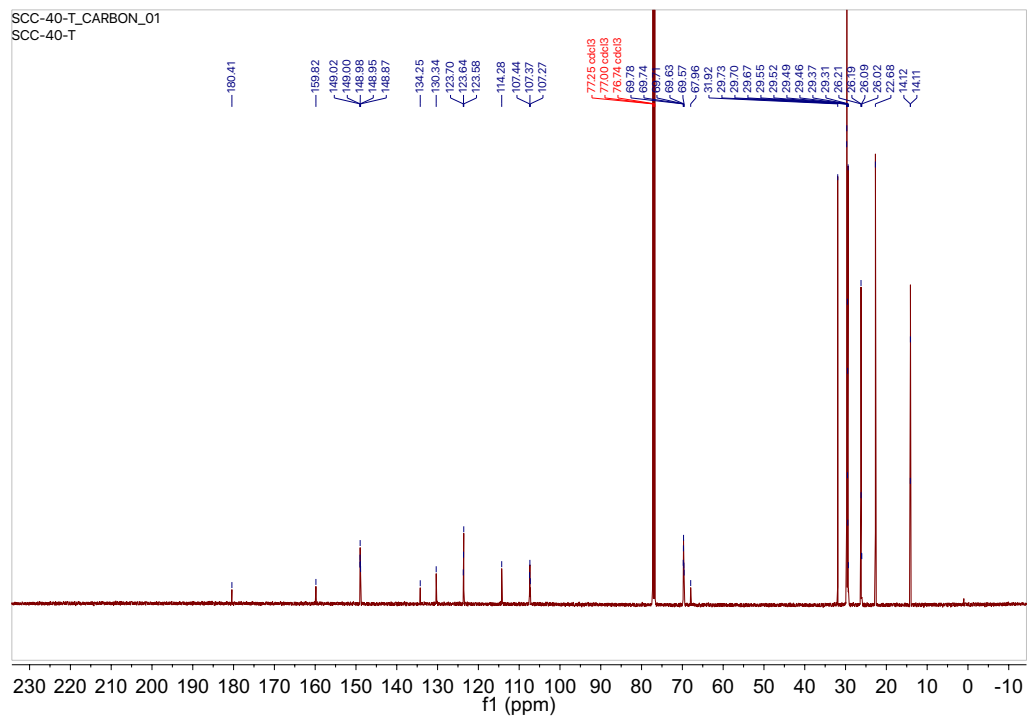
Figure S14: $^{13}C\{^1H\}$ NMR spectrum of **5.**
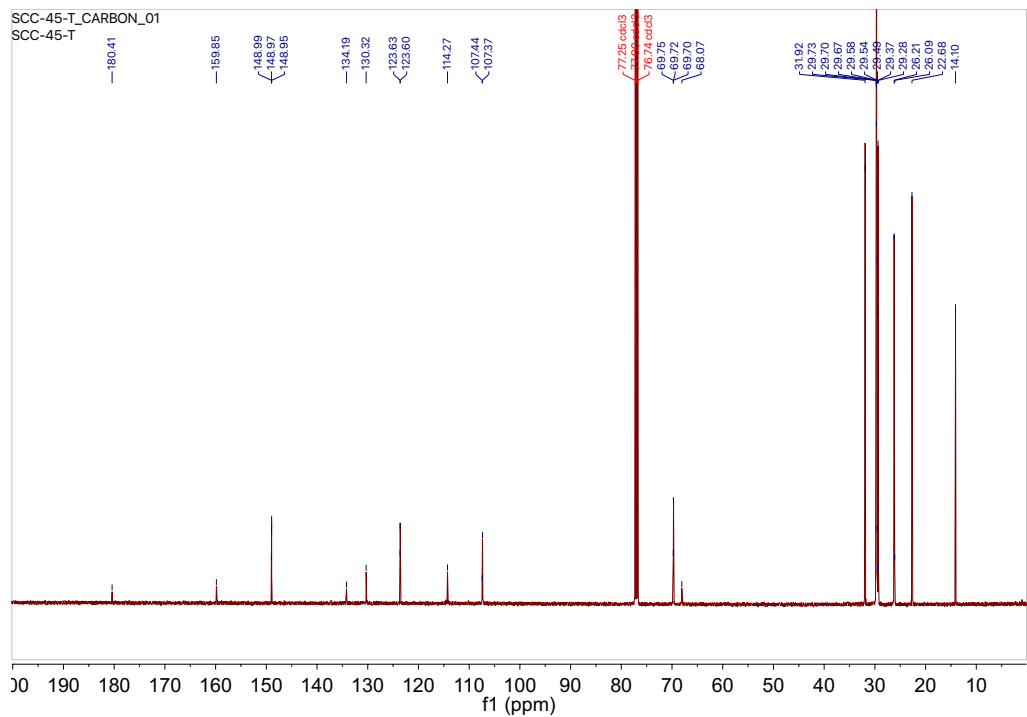
Figure S15: $^{13}C\{^1H\}$ NMR spectrum of **6.**

UV-Visible and luminescence data

Table S1. UV-Visible and luminescence data for the benzil precursors, and for the nickel complexes, in dichloromethane solution at 298 K (2 x 10^{-6} M).

Compound	λ /nm (ε/ 10^3 M^{-1} cm^{-1})	$\lambda_{max, ex}$ (nm)	$\lambda_{max,em}$ (nm)	τ_{av}[a] (ns)	τ_n[b] ; A_n[c]	QY (%)[d]
1	279 (249.1), 310 (83.5)	278	388	6.85	τ_1 = 1.16 ; A_1 = 34.13 τ_2 = 7.32 ; A_2 = 65.87	3.34
2	279 (212.1), 310 (73.5)	278	388	5.14	τ_1 = 2.10 ; A_1 = 87.92 τ_2 = 9.86 ; A_2 = 12.08	5.12
3	279 (214.4), 310 (68.3)	278	388	3.86	τ_1 = 3.86 ; A_1 = 100.0	7.78
4	277 (458.5), 306 (152.5), 922 (27.7)	321	388	7.31	τ_1 = 2.05 ; A_1 = 20.42 τ_2 = 7.67 ; A_2 = 79.58	2.69
5	277 (520.0), 304 (169.0), 918 (23.3)	321	388	6.46	τ_1 = 1.46 ; A_1 = 26.75 τ_2 = 6.85 ; A_2 = 73.25	4.75
6	279 (437.4), 310 (139.4), 918 (24.6)	321	388	5.95	τ_1 = 1.99 ; A_1 = 31.99 τ_2 = 6.52 ; A_2 = 68.01	6.38

[a] Average lifetime τ_{av} = $(A_1\tau_1^2 + A_2\tau_2^2 + \cdots)/((A_1\tau_1 + A_2\tau_2 + \cdots)$ ($\pm$ 0.03). [b] τ_n = Natural lifetime. [c]

An = Intensity coefficients. [d] Absolute Quantum Yields φ using an integrating sphere ($\pm$ 3%)

UV-Visible spectra in dichloromethane solution (10^{-6} M)
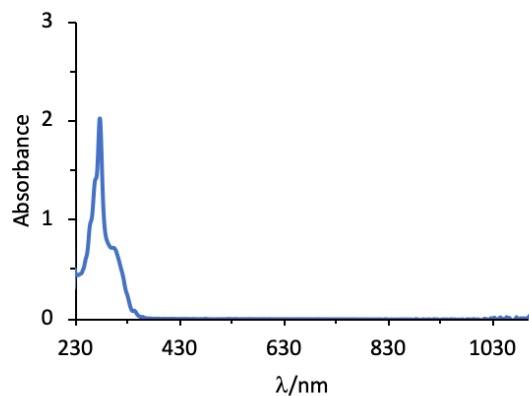
Figure S16. UV-Visible spectra of **1**
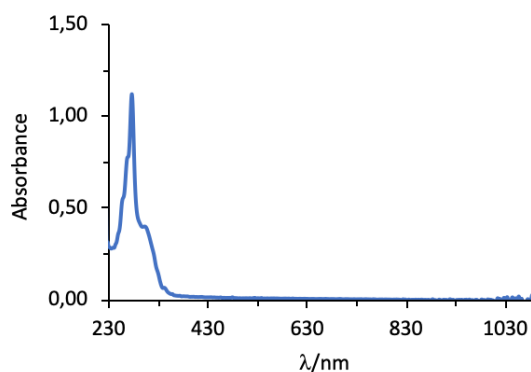
Figure S17. UV-Visible spectra of **2**
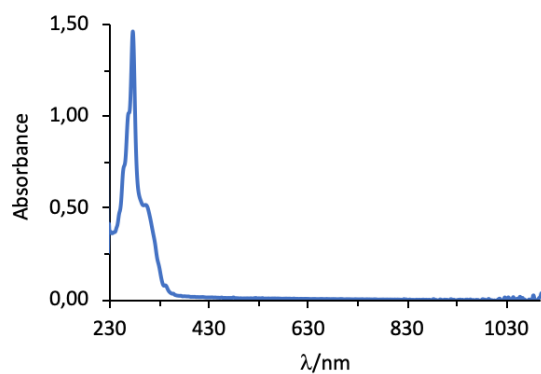
Figure S18. UV-Visible spectra of **3**
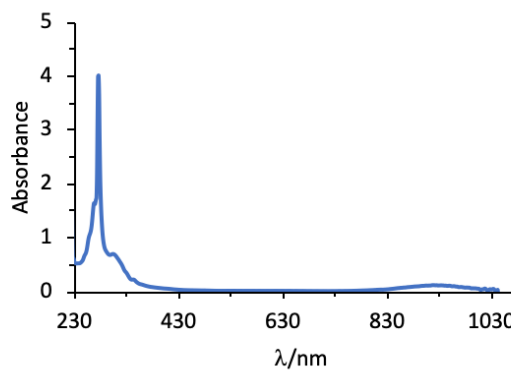
Figure S19. UV-Visible spectra of **4**
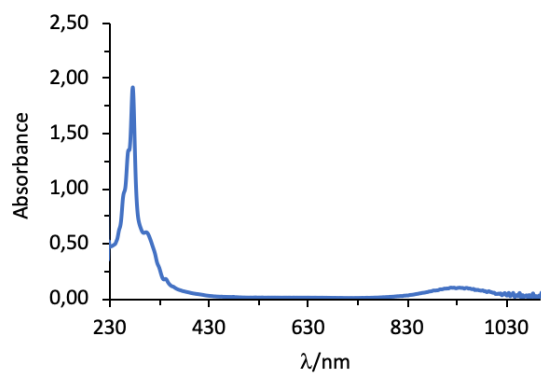
Figure S20. UV-Visible spectra of **5**
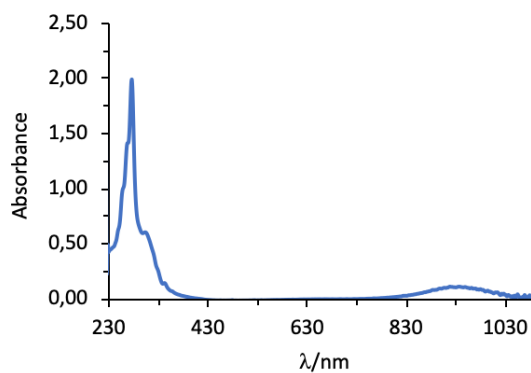
Figure S21. UV-Visible spectra of **6**

Luminescence spectra: Excitation (left) and emission (right) spectra recorded in CH_2Cl_2 solution (10^{-5} M) at room temperature.
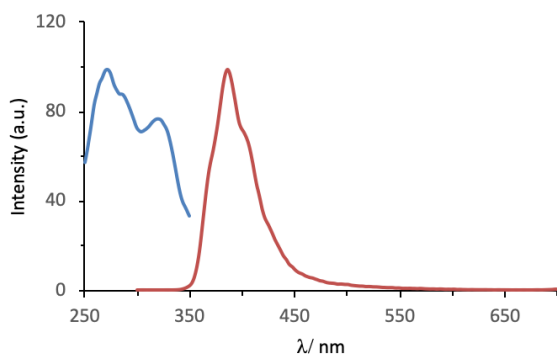
Figure S22. Luminescence spectra for **1.**
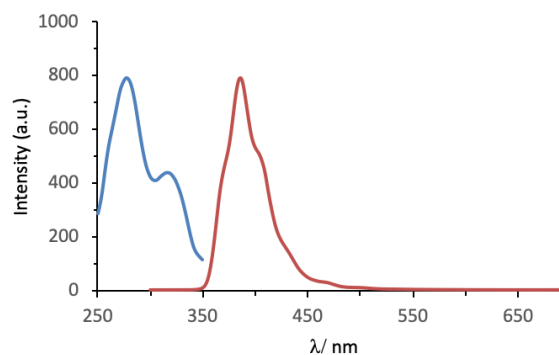
Figure S23. Luminescence spectra for **2.**
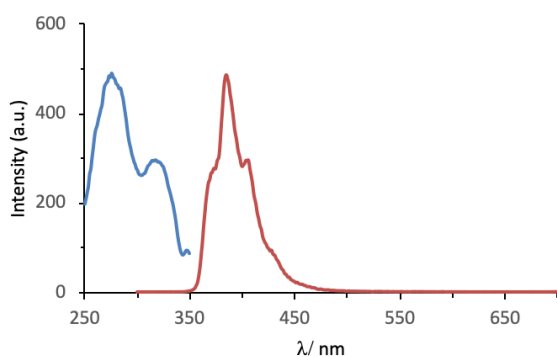
Figure S24. Luminescence spectra for **3.**
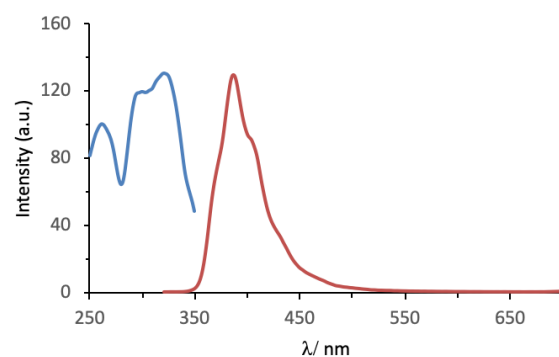
Figure S5. Luminescence spectra for **4.**
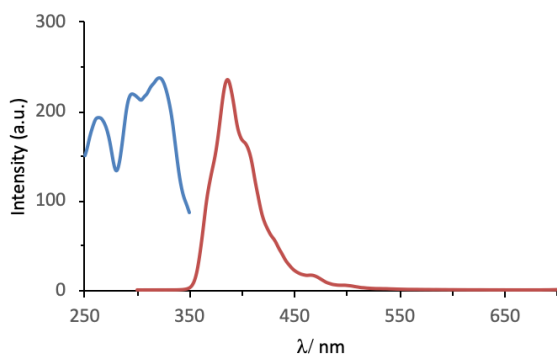
Figure S26. Luminescence spectra for **5.**
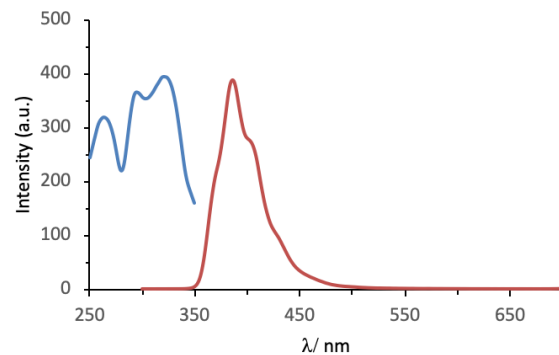
Figure S27. Luminescence spectra for **6.**

Fluorescence lifetimes

Fluorescence decays in dichloromethane, at room temperature. Lifetimes were obtained with the Time Correlated Single Photon Counting (TCSPC) and MCP-PMT counter module (TCC2) of the FLS980 spectrometer. Fluorescence decays were analyzed with the method of non-linear least squares iterative deconvolution ant the quality of the fits was judged by the values of the reduced Chi-square (c2) and the autocorrelation function of the residuals using the FAST (Advanced Fluorescence Lifetime Analysis Software) program provided by the equipment.
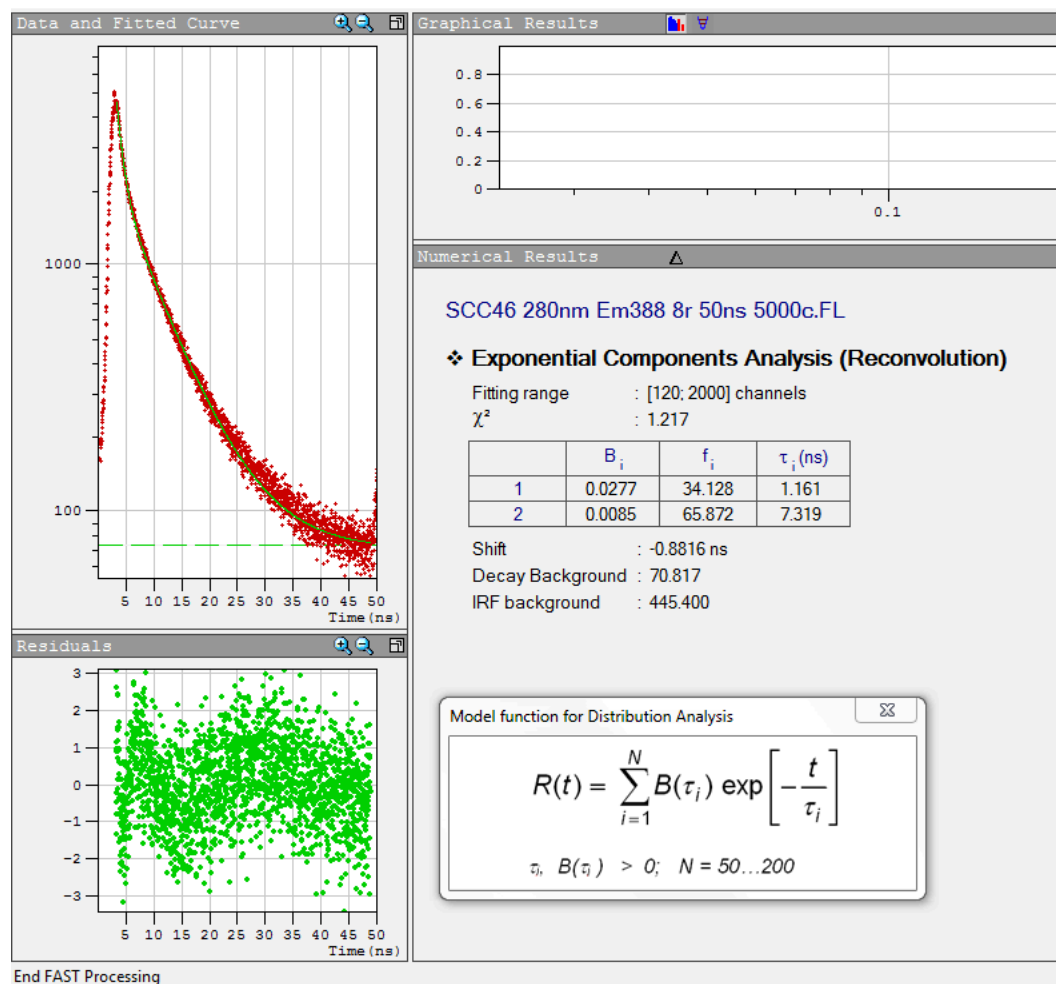
Figure S28. Fluorescence decay for **1** (CH$_2$Cl$_2$)**.** Measurement Conditions: EPL280, MCP-PMT λex = 280 nm, Δλem = 8 nm, pulse 50 ns 5000c λem =388 nm
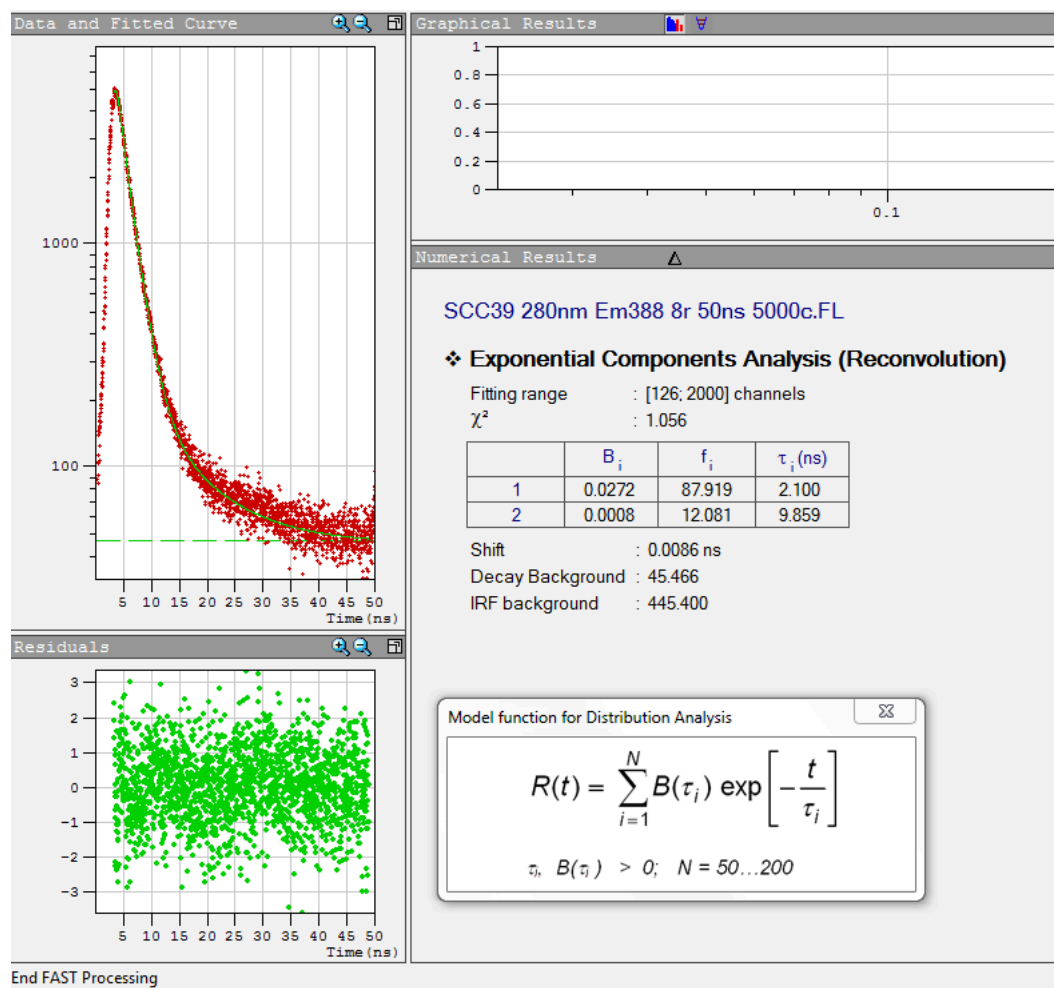
Figure S29. Fluorescence decay for **2** (CH$_2$Cl$_2$)**.** Measurement Conditions: EPL280, MCP-PMT λex = 280 nm, Δλem = 8 nm, pulse 50 ns 5000c λem =388 nm.
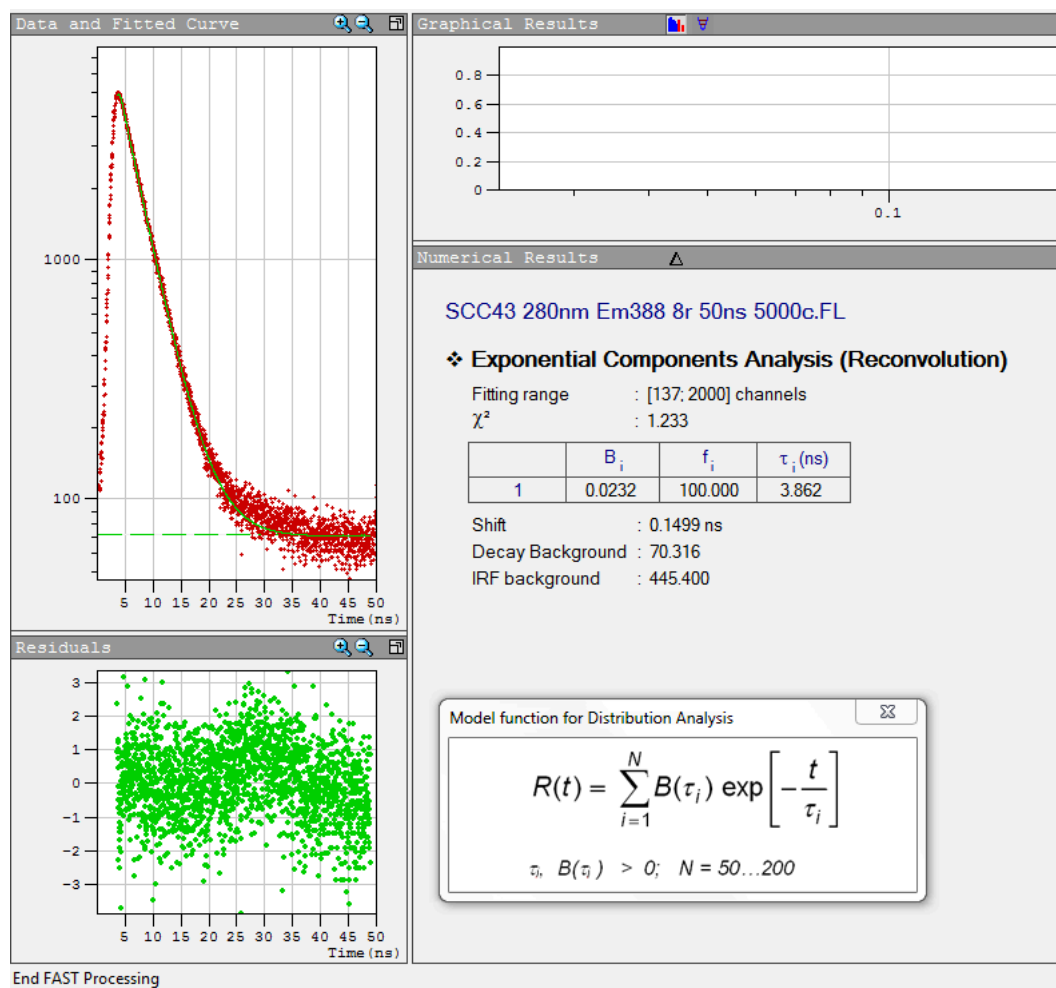
Figure S30. Fluorescence decay for **3** (CH₂Cl₂)**.** Measurement Conditions: EPL280, MCP-PMT λex = 280 nm, $\Delta\lambda$em = 8 nm, pulse 50 ns 5000c λem =388 nm.
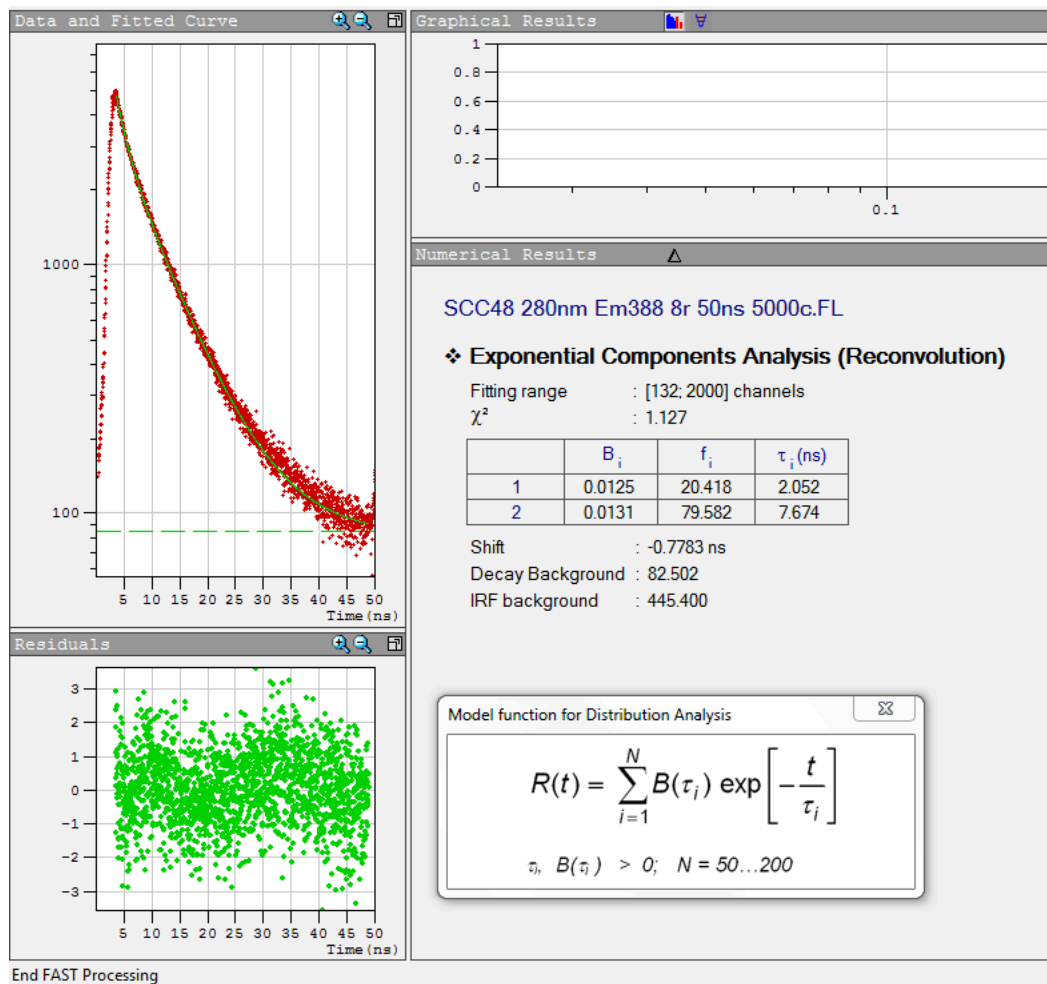
Figure S31. Fluorescence decay for **4** (CH$_2$Cl$_2$)**.** Measurement Conditions: EPL280, MCP-PMT λex = 280 nm, $\Delta\lambda$em = 8 nm, pulse 50 ns 5000c λem =388 nm.
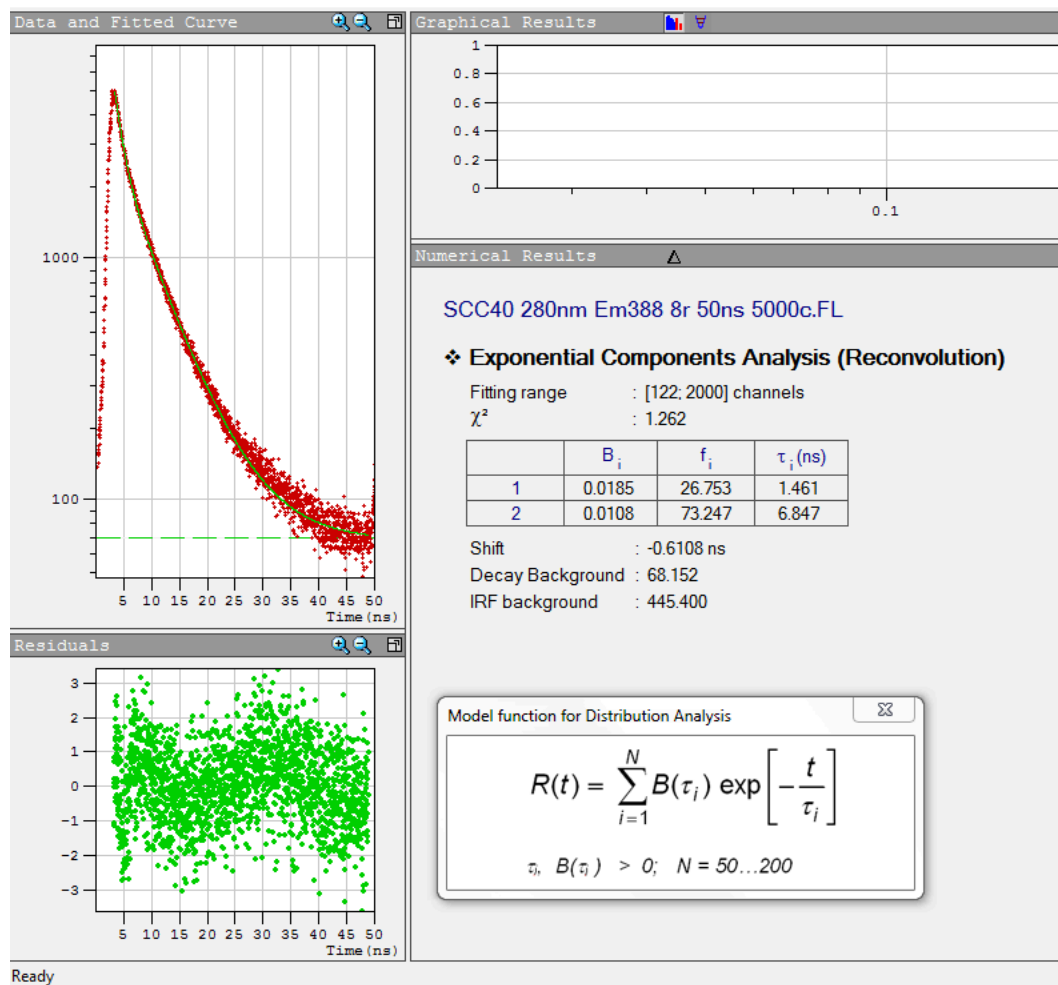
Figure S32. Fluorescence decay for **5** (CH₂Cl₂)**.** Measurement Conditions: EPL280, MCP-PMT λex = 280 nm, Δλem = 8 nm, pulse 50 ns 5000c λem =388 nm.
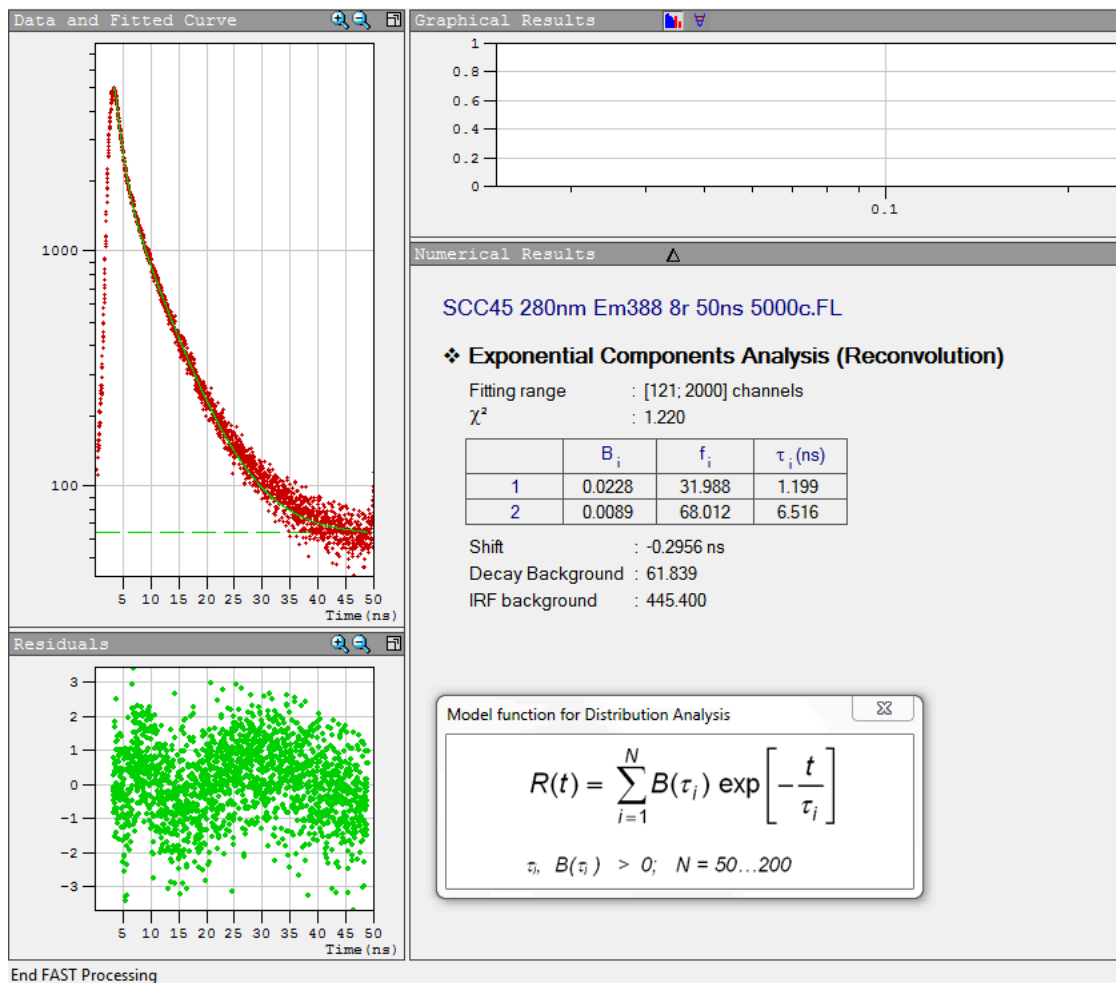
Figure S33. Fluorescence decay for **6** (CH₂Cl₂)**.** Measurement Conditions: EPL280, MCP-PMT λex = 280 nm, Δλem = 8 nm, pulse 50 ns 5000c λem =388 nm.

Absolute Quantum Yields φ using an integrating sphere (± 3%)
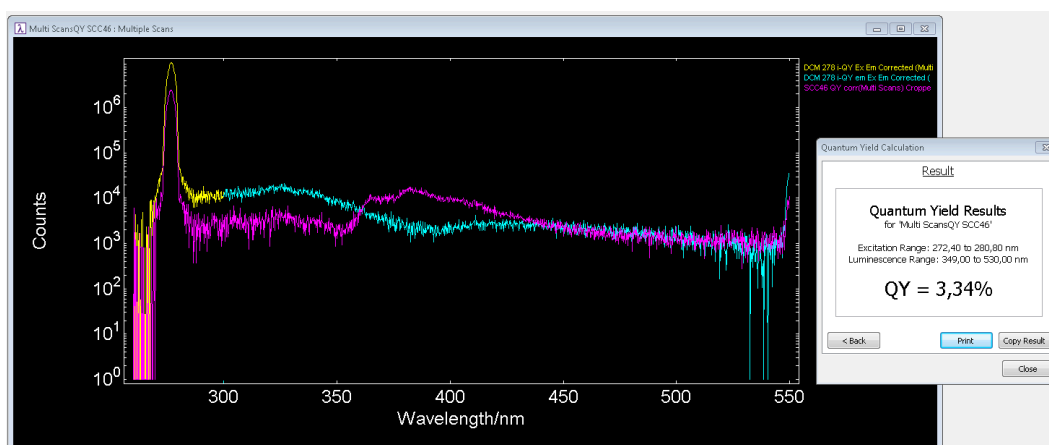
Figure S34. Quantum Yield for **1.** Measurement conditions: λex = λem = 278 nm, Δλexc = 3 nm, Δλem = 0,2nm step = 0.2nm, dwell = 0,3 s repetitions 3.
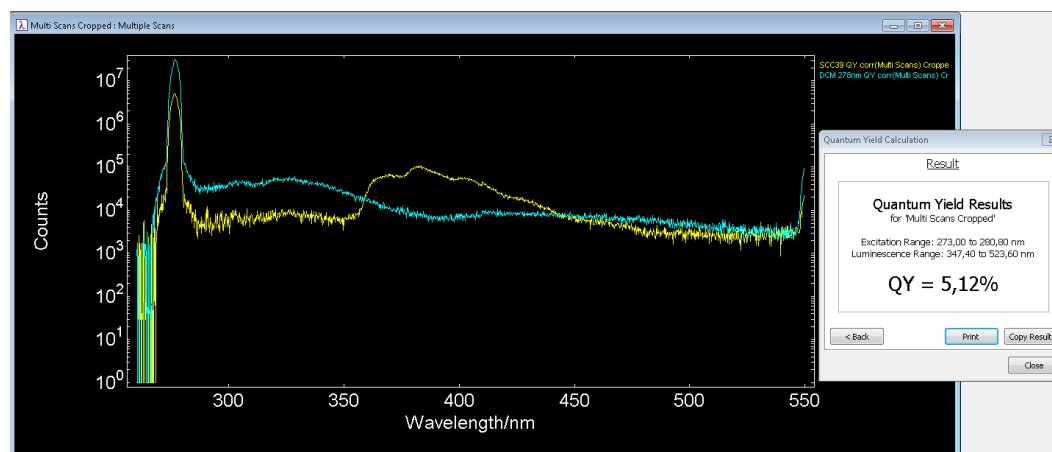
Figure S35. Quantum Yield for **2.** Measurement conditions: λex = λem = 278 nm, Δλexc = 3 nm, Δλem = 0,2nm step = 0.2nm, dwell = 0,3 s repetitions 3.
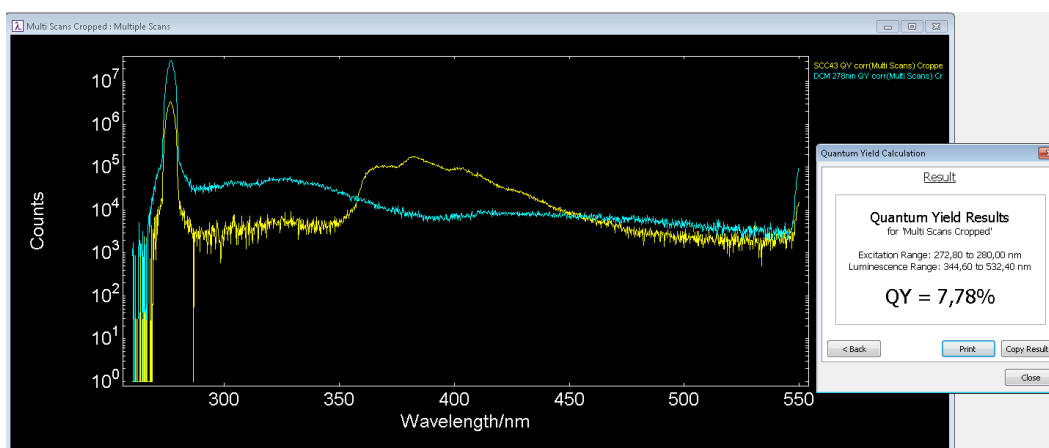
Figure S36. Quantum Yield for **3.** Measurement conditions: λex = λem = 278 nm, Δλexc = 3 nm, Δλem = 0,2nm step = 0.2nm, dwell = 0,3 s repetitions 3.
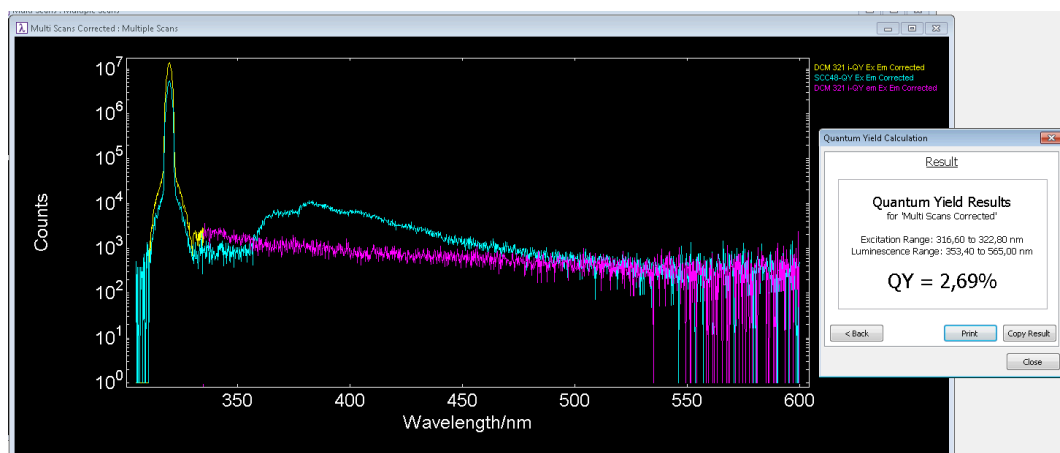
Figure S37. Quantum Yield for **4.** Measurement conditions: λex = λem = 278 nm, Δλexc = 3 nm, Δλem = 0,2nm step = 0.2nm, dwell = 0,3 s repetitions 3.
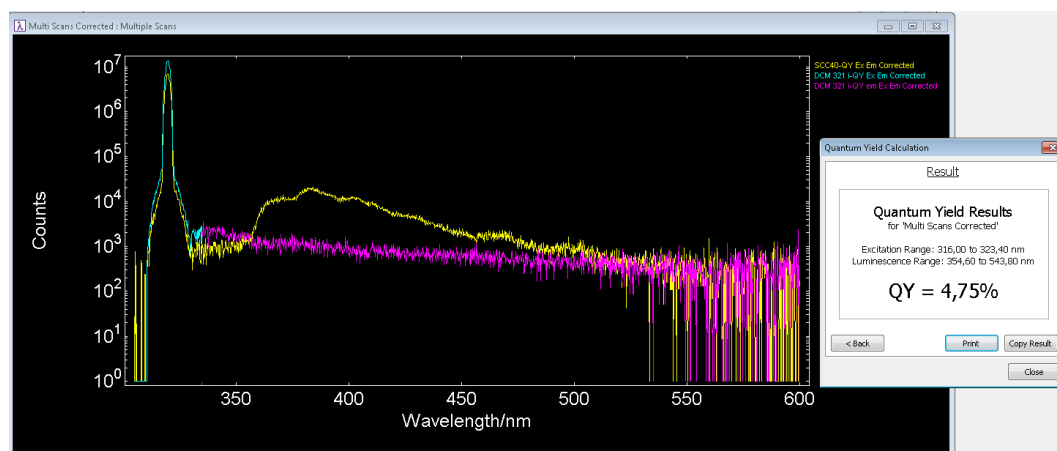
Figure S38. Quantum Yield for **5.** Measurement conditions: λex = λem = 278 nm, Δλexc = 3 nm, Δλem = 0,2nm step = 0.2nm, dwell = 0,3 s repetitions 3.
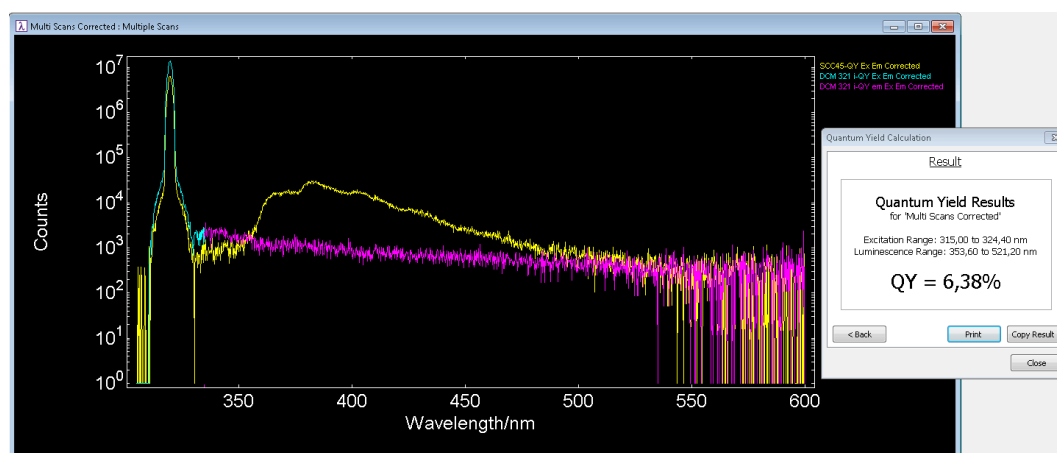
Figure S39. Quantum Yield for **6.** Measurement conditions: λex = λem = 278 nm, Δλexc = 3 nm, Δλem = 0,2nm step = 0.2nm, dwell = 0,3 s repetitions 3.

MALDI-TOF mass spectra

Meas. m/z	m/z	err [ppm]	Ion Formula
2,624.0889	2624.0934	-4.5	C174H278O16

$[M]^+$
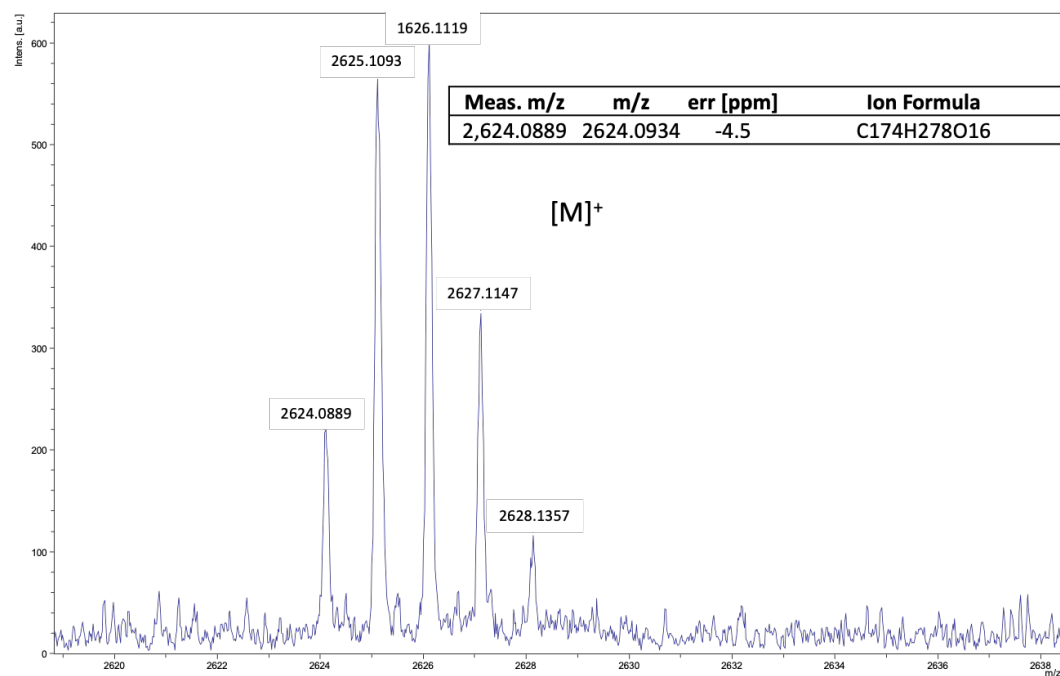
Figure S40: MALDI-TOF mass spectrum of **1.**

Meas. m/z	m/z	err [ppm]	Ion Formula
2,736.2224	2736.2186	3.8	C182H294O16

$[M]^+$
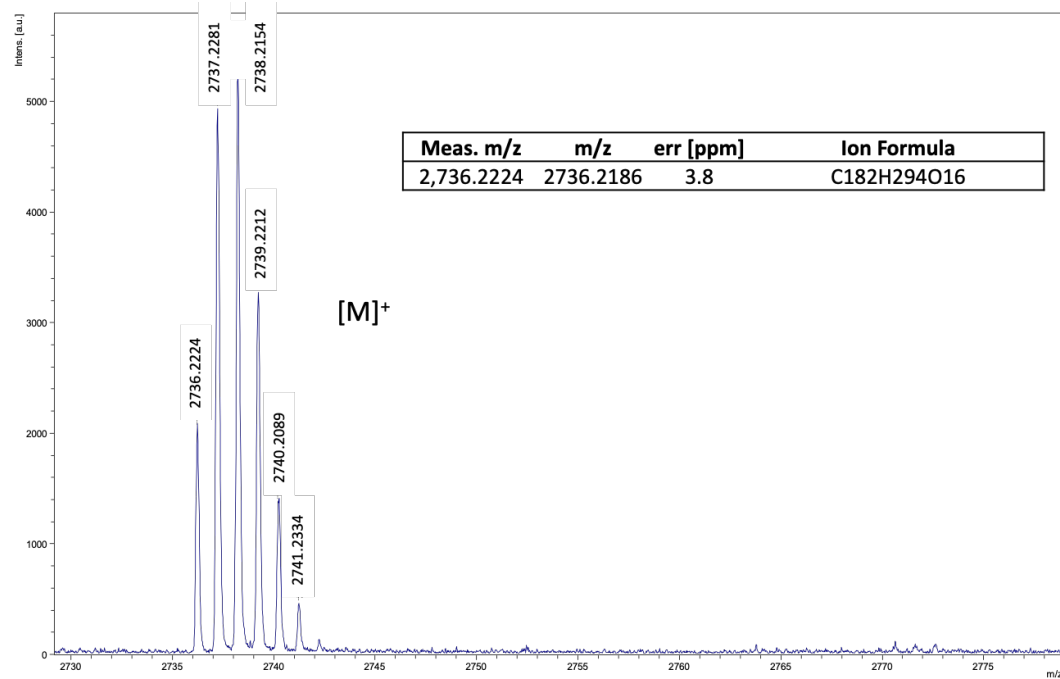
Figure S41: MALDI-TOF mass spectrum of **2.**

Meas. m/z	m/z	err [ppm]	Ion Formula
2848.3485	2848.3438	4.7	C190H310O16
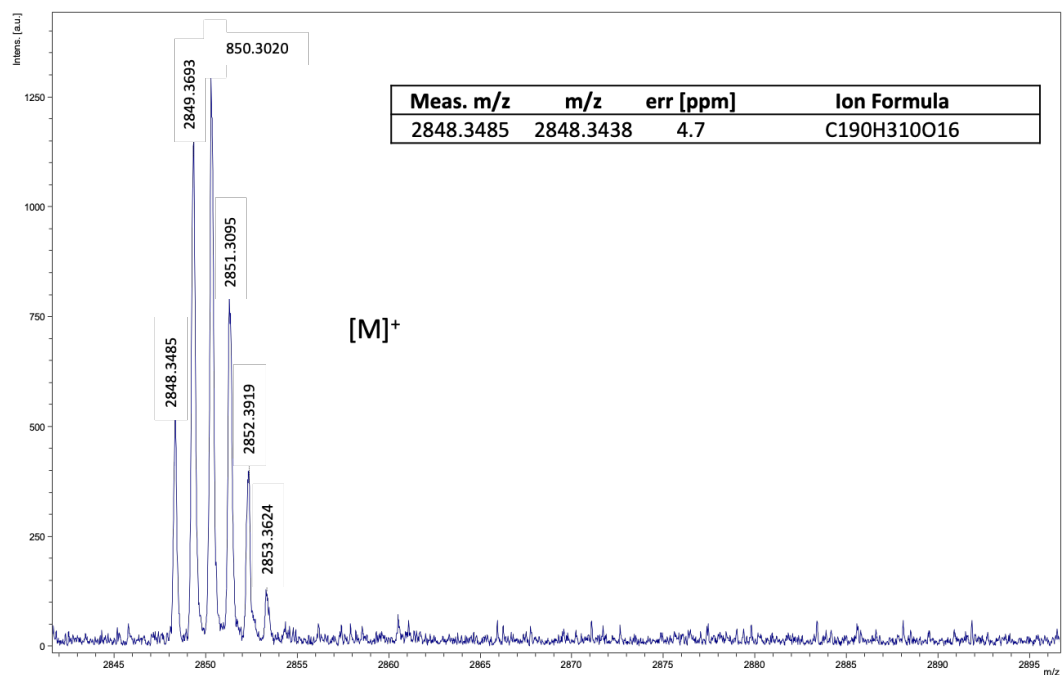
Figure S42: MALDI-TOF mass spectrum of **3.**

Meas. m/z	m/z	err [ppm]	Ion Formula
5,370.0510	5370.0314	19.6	C348H556NiO28S4
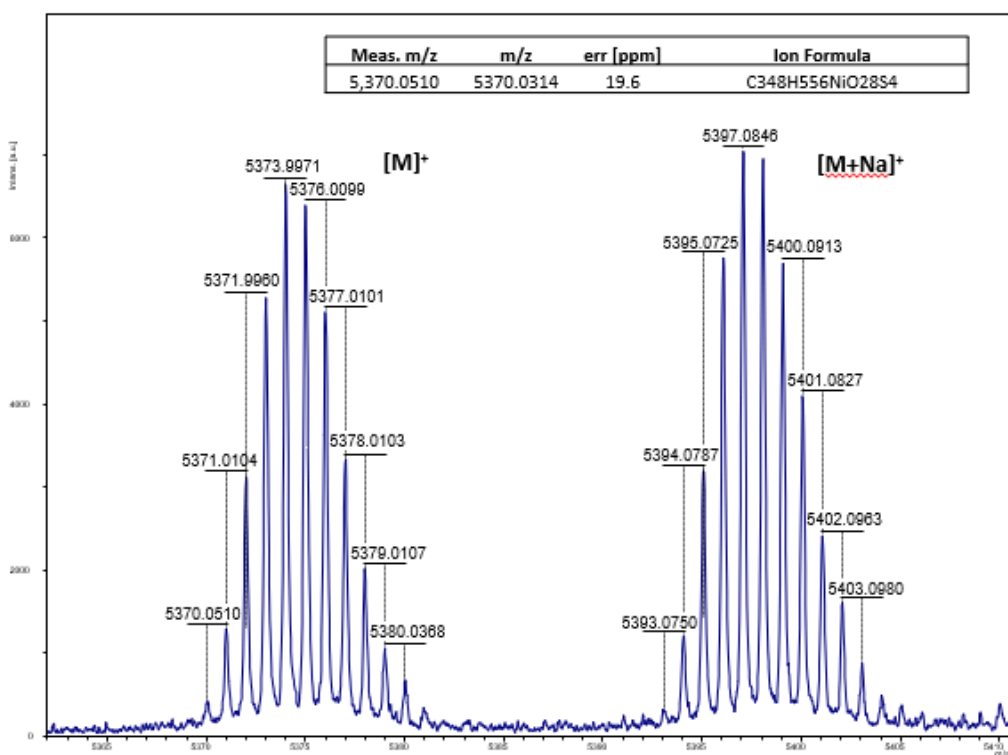
Figure S43: MALDI-TOF mass spectrum of **4.**
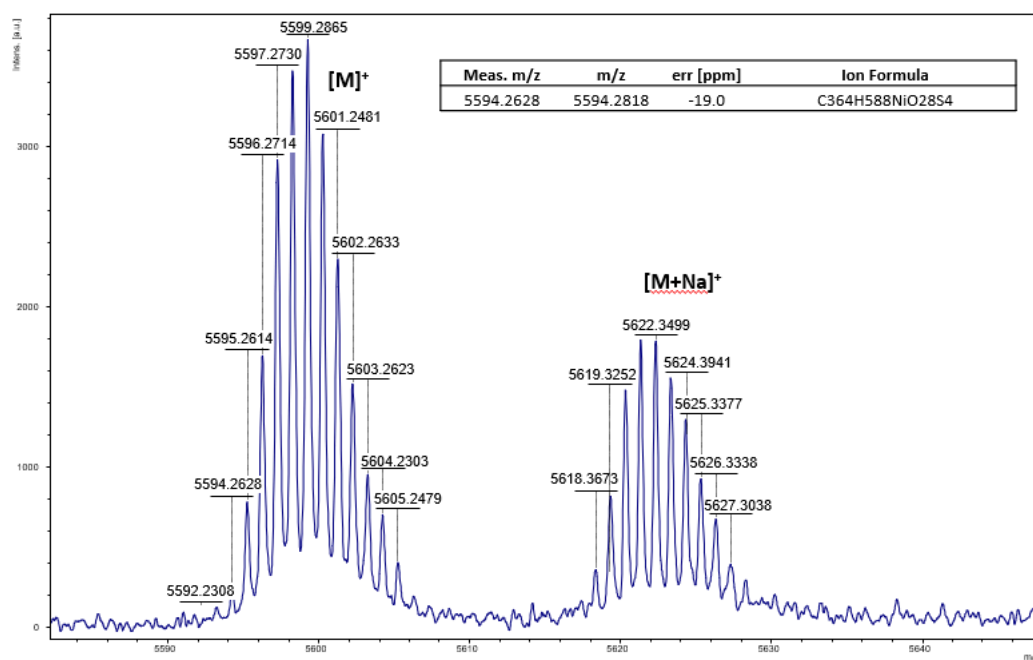
Figure S44: MALDI-TOF mass spectrum of **5.**
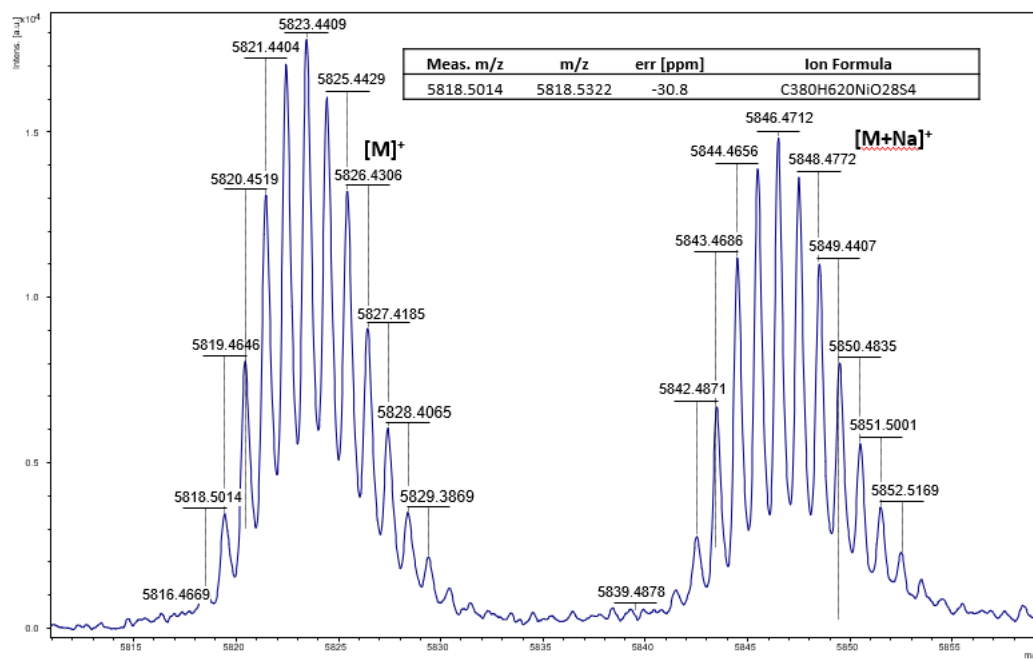
Figure S45: MALDI-TOF mass spectrum of **6.**

DSC scans. From top to bottom : first heating, first cooling, second heating.
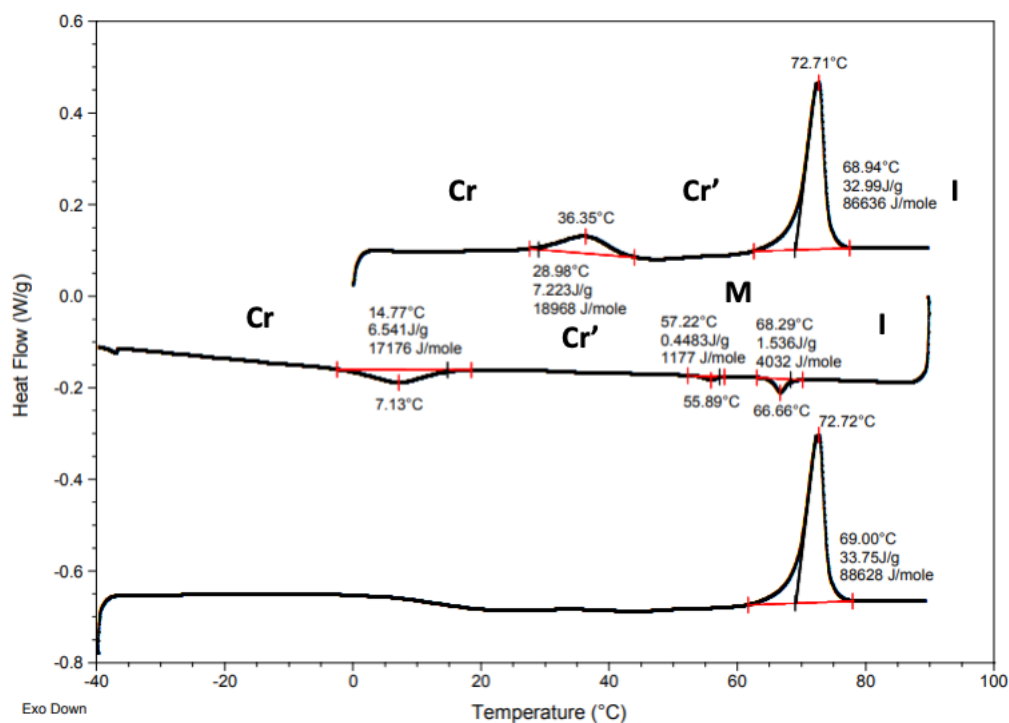
Figure S46: DSC scans of **1**.
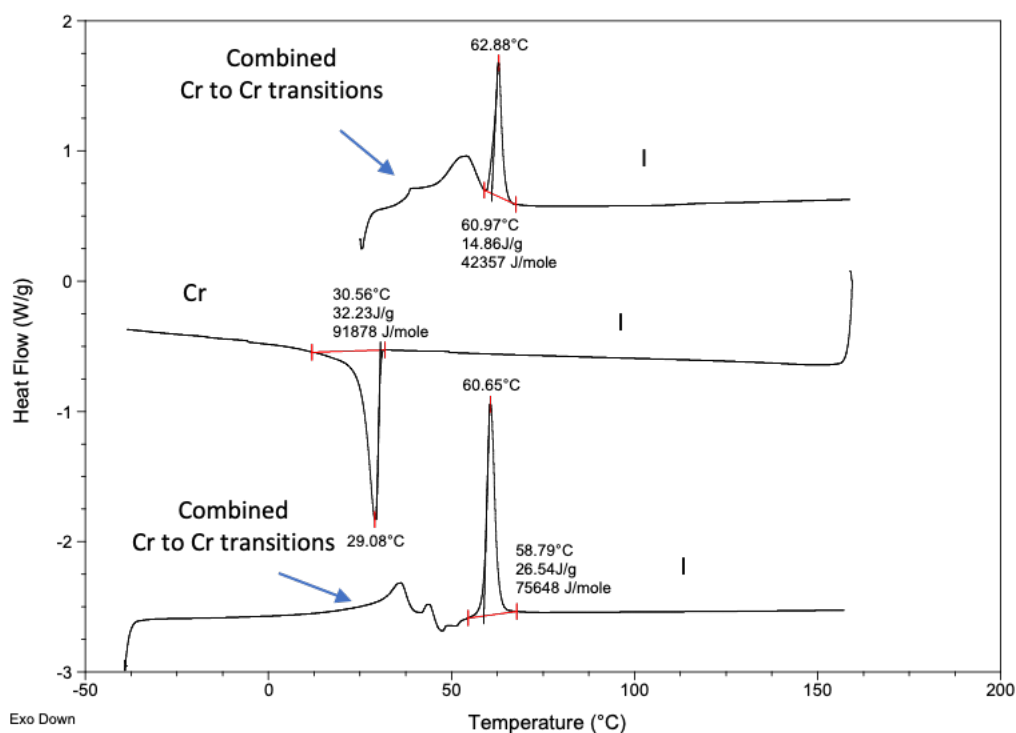
Figure S47: DSC scans of **2.**
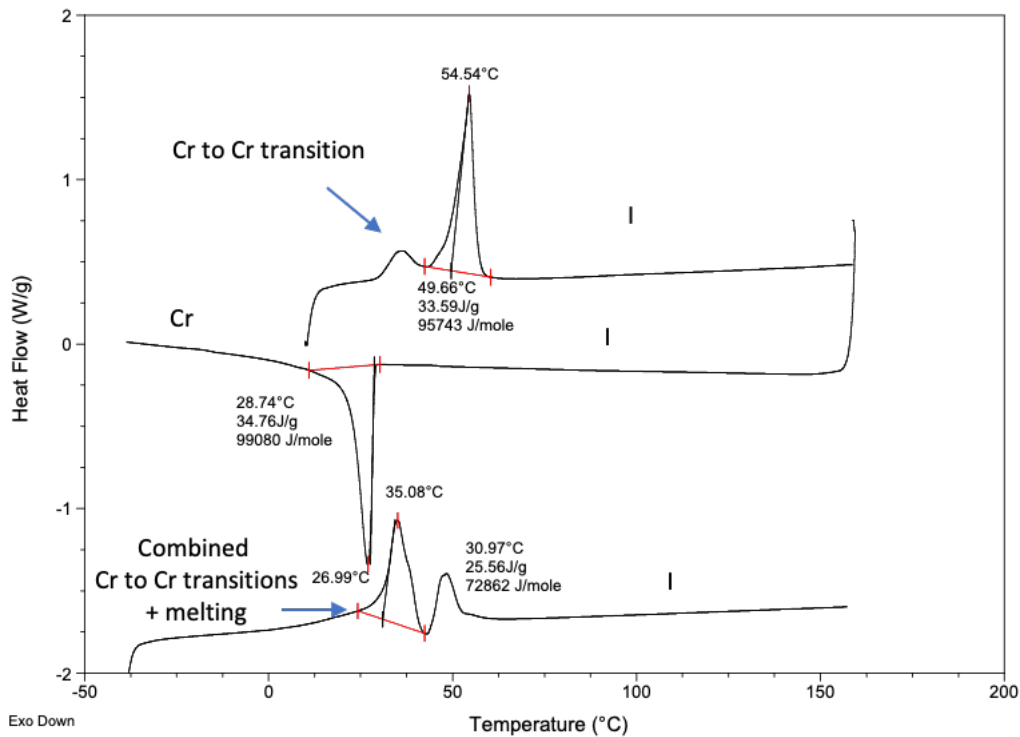
Figure S48: DSC scans of **3.**
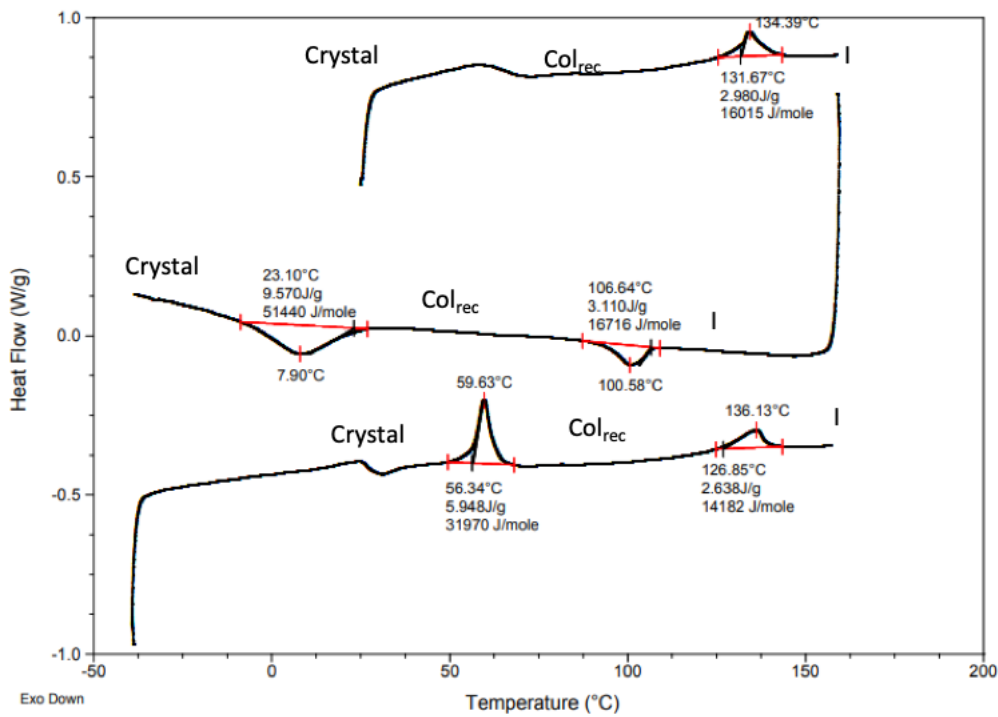
Figure S49: DSC scans of **4.**
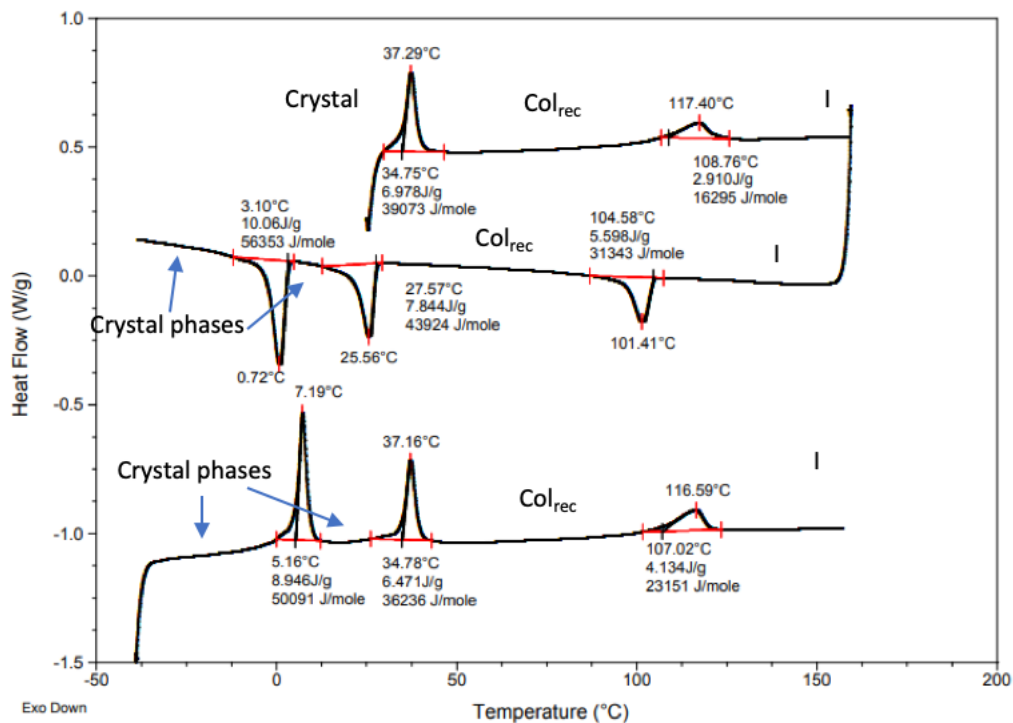
Figure S50: DSC scans of **5.**
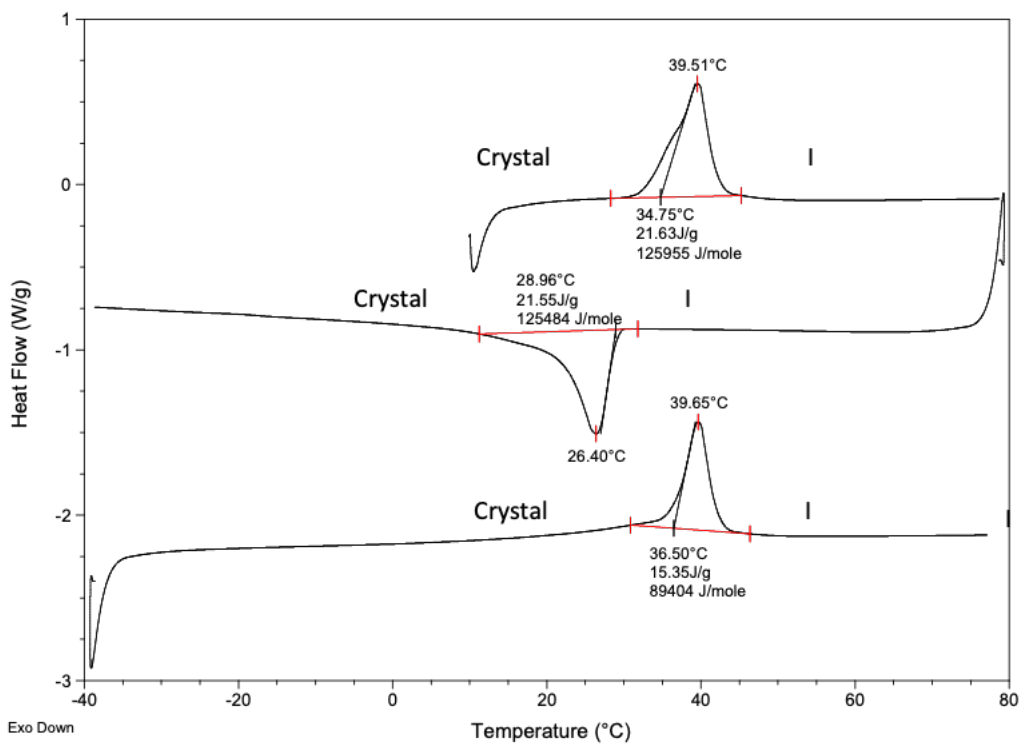
Figure S51: DSC scans of **6.**

Thermogravimetric analysis
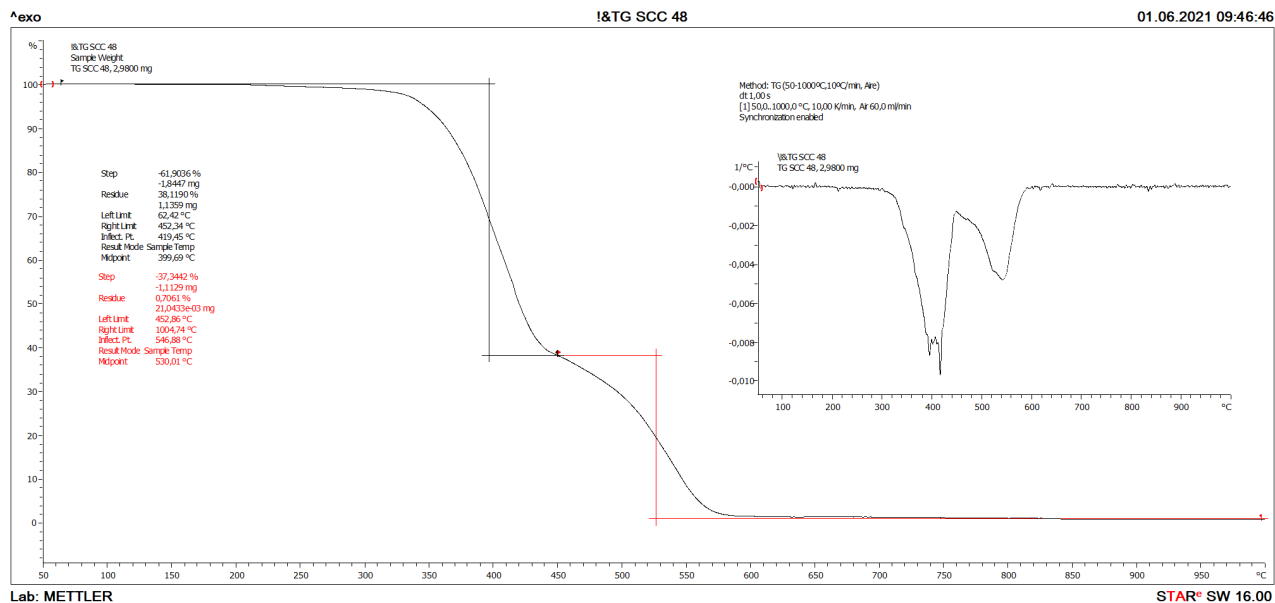
Figure S52: TGA scan of **4.**
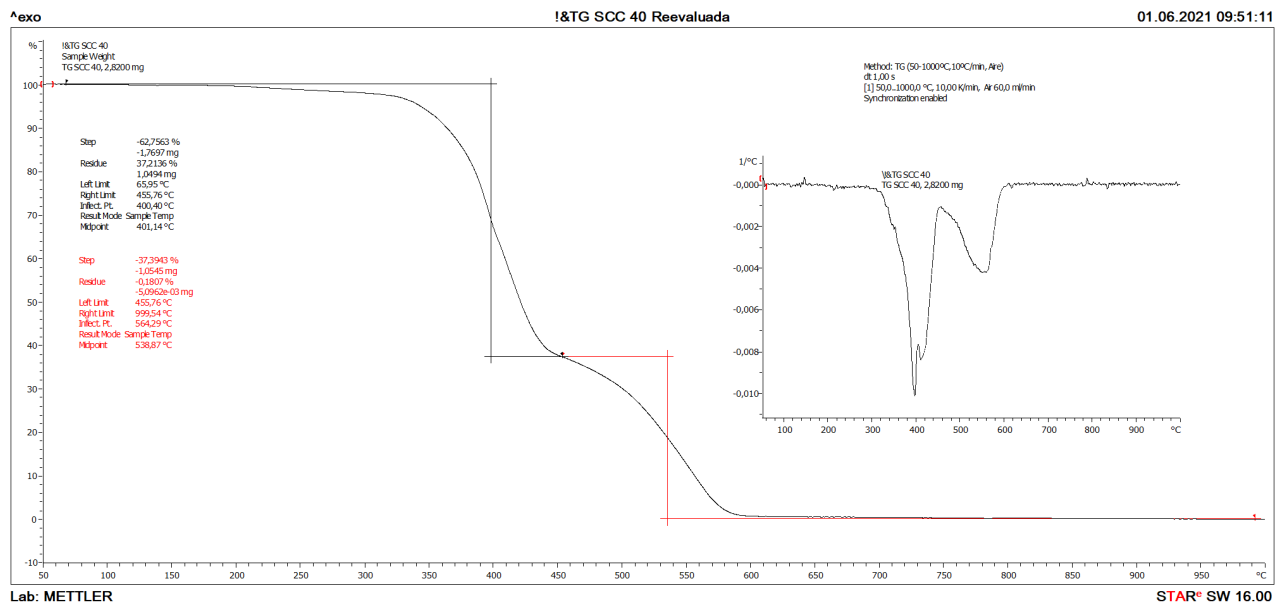
Figure S53: TGA scan of **5.**
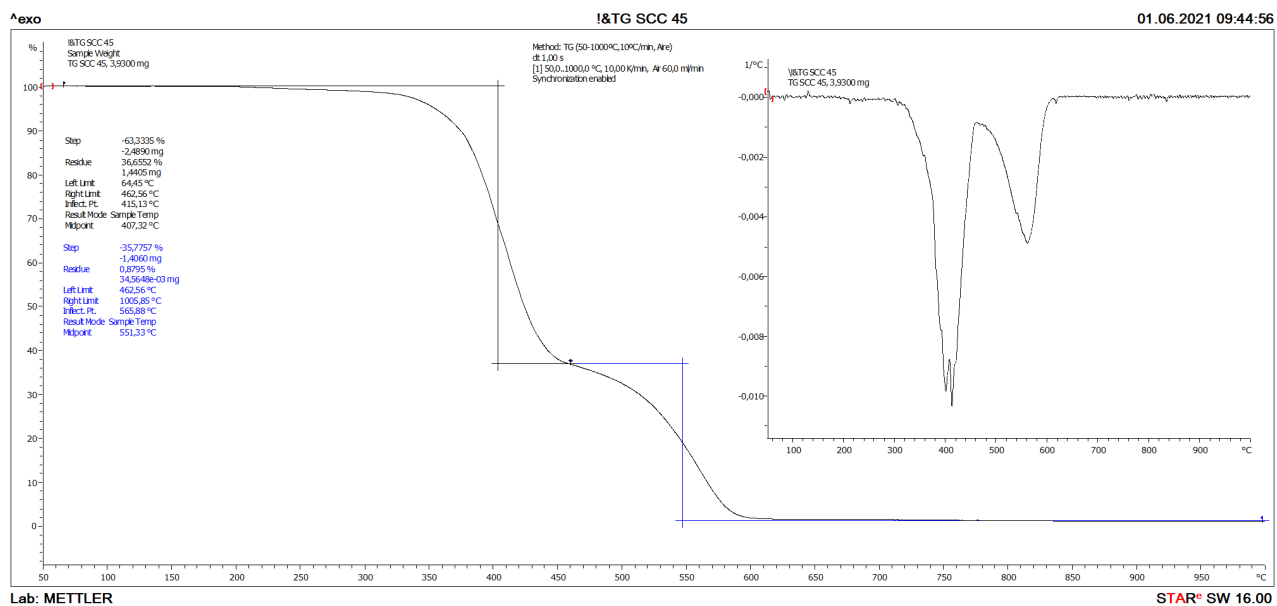
Figure S54: TGA scan of **6.**

X-ray diffraction measurements

The diffraction diagrams were recorded using a Stoe Stadivari goniometer equipped with a Genix3D microfocus generator (Xenocs) and a Dectris Pilatus 100K detector. Temperature control was achieved using a nitrogen-gas Cryostream controller (Oxford Cryosystems) allowing for a temperature control of about 0.1 ºC. The materials were enclosed in capillary tubes of 0.6 mm of diameter. The exposure time was 5 minutes. Monochromatic Cu-Kα radiation ($\lambda = 1.5418$ Å) was used.

Procedure to obtain charge-density maps

Our strategy for structure characterization consisted in the construction of electron density maps (Fourier maps) $\rho(x, y)$ using the diffracted intensities after indexing the X-ray diagram. If only $(h, k, 0)$ reflections are considered the maps represent a projection of the structure along the c axis with no information concerning the periodicity along c. However, we can obtain a completely reliable image of the structure by positioning the molecules in the (a, b) unit cell. The procedure is based on the inverse Fourier transform of the diffraction diagram. Briefly, the intensity of a given $(h, k, 0)$ reflection is proportional to the square modulus of the complex $(h, k, 0)$ Fourier amplitude of the periodic electron density of the structure. The technical details of the procedure to obtain the charge-density map are described elsewhere.[2] The procedure can be carried out if $\rho(x, y) = \rho(-x, -y)$ for a given origin of the unit cell, *i.e.* when the layer group of the structure contains inversion centers or two-fold axes perpendicular to the lattice plane, as is the case of practically the whole set of structural models proposed up to now. In this situation the structure factors are real, their moduli are the square root of the intensities (once corrected from the geometrical factors that are inherent to our experiment), and only their signs are to be determined. It is worth noting that the method has some ambiguity, because the phases $(0$ or $\pi)$ of the different Fourier components are not experimentally accessible. As a consequence, more than one map can be compatible with the

X-ray pattern of a compound. The correct sign combination is decided by the physical merit of the obtained density map, taking into account the packing conditions, molecular sizes and optimization of the steric interactions.
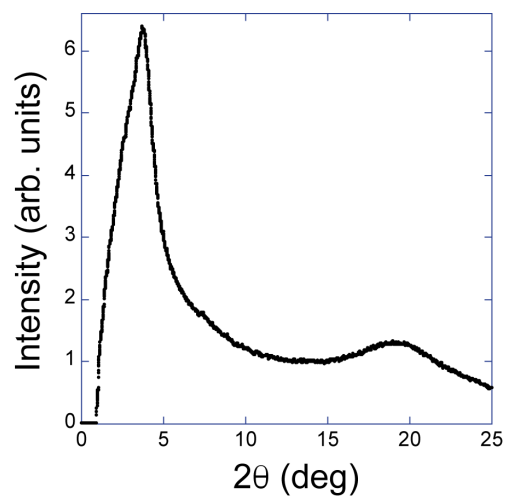
Figure S55. X-ray pattern of **1** at the I phase (90 ºC).
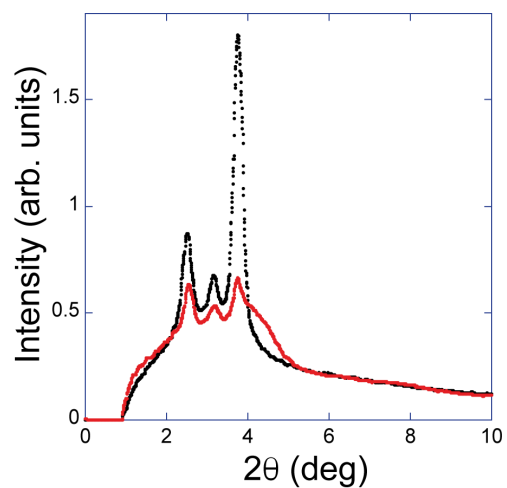
Figure S56. X-ray pattern of **1** at the small angle region showing two crystalline phases at 50 ºC (black curve) and 10 ºC (red curve).
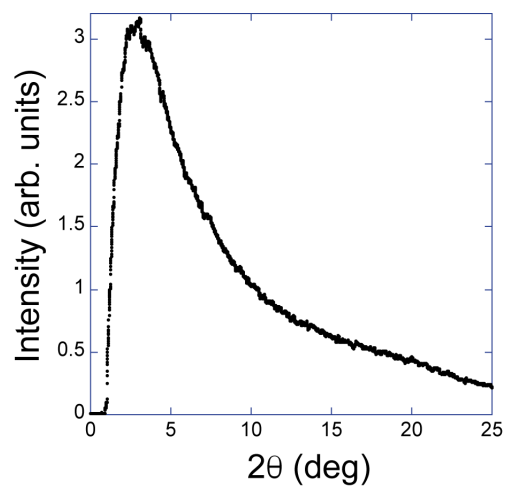
Figure S57. X-ray pattern of **4** at the I phase (145 ºC).
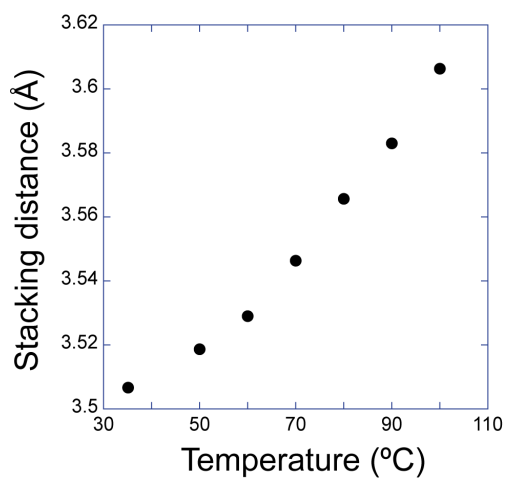
Figure S58. Temperature dependence of the stacking distance in the Col$_{rec}$ phase of **5**.
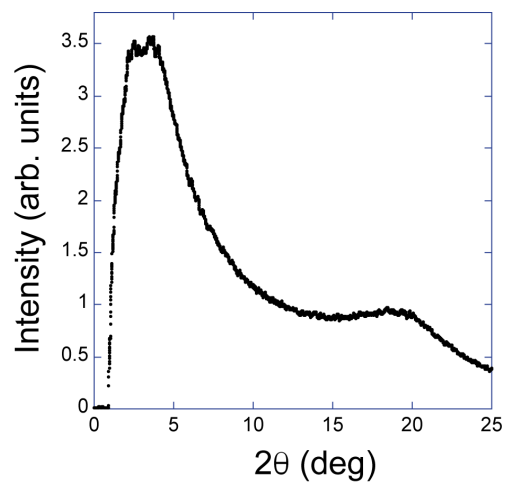
Figure S59. X-ray pattern of **5** at the I phase (140 ºC).
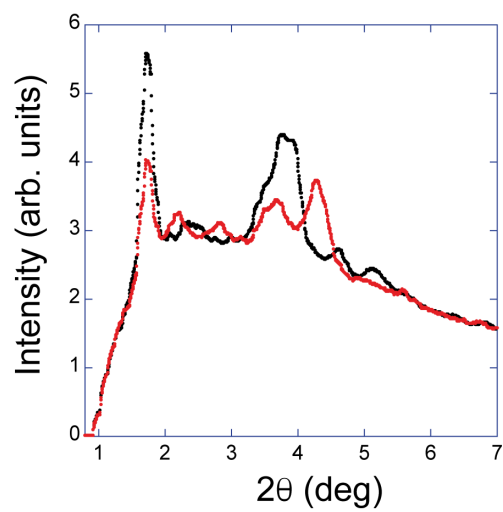
Figure S60. X-ray pattern at the small-angle region of the two crystalline phases of **5** (black curve 20 ºC, red curve -5 ºC).

Computational Details

Theoretical methods have been applied to obtain information on both the structural and electronic properties. Since no important differences are expected with respect to the length distance between the organic and metal-organic fragments, theoretical calculations have only been carried out for a simplified model of complex **4**. Furthermore, the alkoxy pendant chains are responsible for the fluidity of the mesophase. But we are focused on properties that mainly arise from triphenylene and / or metal-organic fragments. Therefore, OR pendant groups were replaced with methoxy groups.[3]

Due to the large number of atoms in the system (277 atoms per molecule) and the presence of transition metals atoms, all geometry optimizations were performed using the GFN2-xTB method.[4] The GFN2-xTB method is an extended semiempirical tight-binding method that has been specifically designed for fast calculation of structures and noncovalent interactions energies for molecular systems with approximately 1000 atoms. This method has demonstrated its ability to accurately describe noncovalent interactions in the context of organic materials,[4,5] transition-metal complexes and organometallic supramolecular structures.[6] All calculations with GFN2-xTB method were done by using the software xTB.[7]

To study electronic absorption properties, vertical transition energies (ΔE_{TD}) were calculated from previously optimized geometries by using Time-Dependent Density Functional Theory (TD-DFT) as implemented in ORCA software.[8] In ORCA, TD-DFT calculations are automatically performed using the Tamm-Dancoff approximation (TDA). Although TDA approach tends to underestimate strength factors (f), it provides accurate results for the band shapes and the position of the absorption peaks compared to experimental UV-Vis absorption spectra, with reduced computational effort.[9] Here, simplified Tamm-Dancoff (sTDA) was used to study electronic

absorption features. The sTDA approach is specifically designed for computing electronic absorption spectra of large molecules with several hundred atoms, while significantly reducing the computational effort compared to conventional TD-DFT (by two or three orders of magnitude), with a minor loss of accuracy.[10] Thus, sTDA approach has allowed us for efficient calculation of absorption properties, where TD-DFT calculations may be computationally prohibitive. In this paper, transition vertical energies were calculated at TD-CAM-B3LYP level in combination with 6-31+G(d,p) basis set for C, H, O, and S atoms and Def2-TVZP (along with its corresponding pseudopotential) for Ni, from now on: TD-CAM-B3LYP/6-31+G(d,p)/Def2-TVZP). Grimme's D3 dispersion corrections with the Becke-Jonson damping functions (D3BJ) were also considered.[11] In terms of accuracy, range separated functionals, such as CAM-B3LYP when combined with Pople's basis sets than include polarization and diffuse functions, have shown to yield converged vertical transitions energies.[12] When specified below, calculations incorporating a solvation model have been also carried out. Employed solvation models depend on the applied theoretical level. Thus, optimization geometries in solvent were performed using a solvation model based on the analytical linearized Poisson-Boltzmann (APLB),[13] which has been parametrized for extended tight binding methods, while TD-DFT calculations were done using the Conductor-like Polarizable Continuum Model (CPCM).[14] Intermolecular interactions were characterized through the analysis of the reduced density gradient (RDG) at low densities,[15] which allows to find noncovalent interactions based on the peaks that appear through a visual analysis. RDG analysis was conducted using the MultiWFN code.[16] All molecular graphs were done with Visual Molecular Dynamics (VMD) program.[17]

In the following sections, we outline the specific details of theoretical approaches used to study the electronic absorption features in solution, the columnar structure in the mesophase, and the absorption properties in the mesophase.

Electronic absorption properties in solution. Firstly, ground state of **4** was optimized using the GFN2-xTB method. Based on the optimized geometry, vertical transition energies were computed TD-CAM-B3LYP. Both, ground state optimized geometry and vertical transitions energies were calculated in solvent (dichloromethane). Table S2 gathers vertical calculated excitation energies (ΔE_{TD}) of **4** in dichloromethane solvent computed at CAM-B3LYP-D3BJ/6-31+G(d,p)/Def2-TZVP. Figure S29 displays the Molecular orbital diagram of **4** calculated at CAM-B3LYP/6-31+G(d,p)/Def2-TZVP in dichloromethane solvent. As stated, the sTDA approach has been applied, while TDA calculations were also carried out as benchmark in this case. Both TDA and sTDA yield good agreement between the experimental and theoretical transitions. With TDA, the most intense vertical transitions were calculated at 282 nm, 305 nm and 936 nm (291 nm, 311 nm, 939 nm with sTDA), which are consistent with the experimental absorptions at 277 nm, 306 nm and 922 nm, respectively). Furthermore, both approaches provide comparable insights into the main molecular orbitals involved in these transitions. Therefore, the combination of CAM-B3LYP-D3BJ/6-31+G(d,p)/Def2-TZVP theoretical level with either TDA and sTDA are able to describe the main electronic absorption features of nickel bis(dithiolene) complexes. Thus, sTDA has been applied to study absorption properties of nickel bis(dithiolene) complexes in solution with a moderate computational cost.

Table S2. Calculated excitations energies (ΔE_{TD}), oscillator strengths (f) and main configuration of **4** computed at CAM-B3LYP-D3BJ/6-31+G(d,p)/Def2-TZVP in dichloromethane by using TDA and sTDA approximations.

TDA			sTDA			Experimental
ΔE_{TD} (nm)[a]	f	Configuration [b, c]	ΔE_{TD} (nm)[a]	f	Configuration [b, c]	(nm) [d]
282	0.6575	H-4 → L+4	291	0.2106	H-4 →L+4	277

| 305 | 0.5789 | H → L+2 | 311 | 0.2596 | H → L+2 | 306 |
| 962 | 0.2126 | H → L | 938 | 0.1069 | H → L | 922 |

^{a} Only main electronic transitions according to absorption spectra in solution are gathered. ^{b} Percentage contribution in parentheses. ^{c} H = HOMO, L = LUMO. ^{d} Experimental values in dichloromethane.
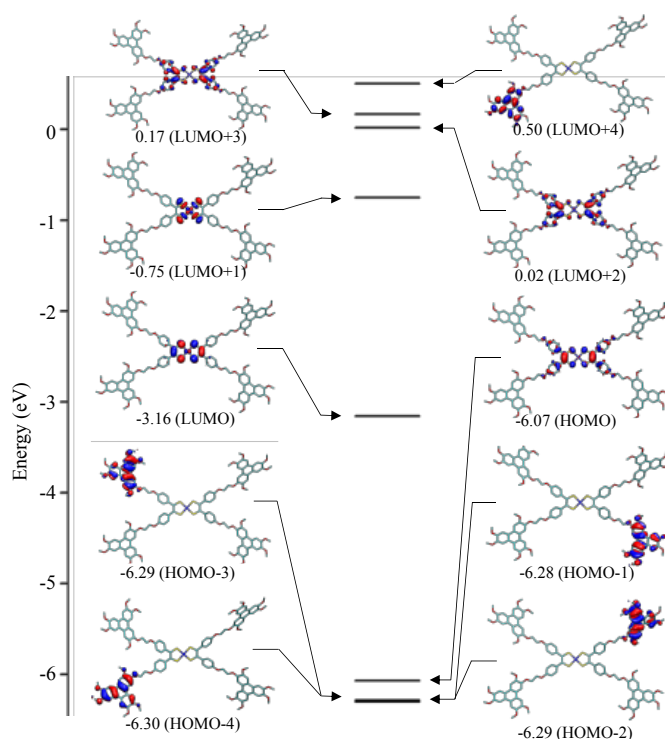
Figure S61. Molecular orbital diagram (isosurface value = 0.03 au) of **4** calculated at CAM-B3LYP-D3BJ/6-31+G(d,p)/Def2-TZVP in dichloromethane solvent. Hydrogen atoms are omitted.

Columnar structure in the mesophase. Supramolecular clusters, containing up to four molecules, were built to study the columnar phase of complex **4** in the mesophase at the molecular level. According to SAXS data, the studied systems were found to stack along the column axis (*z*-axis), exhibiting column segregation between organic and metal-organic fragments. Firstly, to determine the most favourable arrangement between molecules inside the clusters, the evolution of the energy for a couple of molecules was calculated as a function of the azimuthal angle (τ) between them as well as the lateral displacements (Figure S30) through single point calculations. The inter-

molecule distance along z-axis was kept at 3.6 Å. The minimal energy arrangement was found for $\tau = 30°$, x-displacement = 1.2 Å and y-displacement = 0.6 Å. This information was used to generate a dimer, resulting in an optimized structure (Figure S31a) wherein triphenylene rings are co-facially stacked with a distance of 3.7Å ($d_{(TPh-TPh)}$ = 3.7Å), even though there is a lateral displacement. Meanwhile, the metallic fragments associate with each other, leading to Ni-S intermolecular distances (which are parallel to z-axis, $i.e.$ Ni atoms are located over S atoms) around of 3.5 Å ($d_{(Ni-S)}$ = 3.5 Å), while Ni-Ni distance is 4.1 Å ($d_{(Ni-Ni)}$ = 4.1 Å). Furthermore, this information was used to construct a cluster consisting of three molecules. Two possible structures can be constructed depending on the direction of the displacement of the third molecule with respect to the second one: zig-zag and titled (Figure S32b and c), with the titled structure being the most stable. Once again, this structure leads to a co-facial π-stacking between triphenylene rings ($d_{(TPh-TPh)}$ = 3.4 Å) while also exhibiting a lateral displacement. Finally, a titled cluster consisting of four molecules was constructed, which was used here as a model system to study the columnar structure of **4** in the mesophase at the molecular level.

a)

b)

$\tau = 30.0°$ $x = 1.2$ Å $y = 0.6$ Å
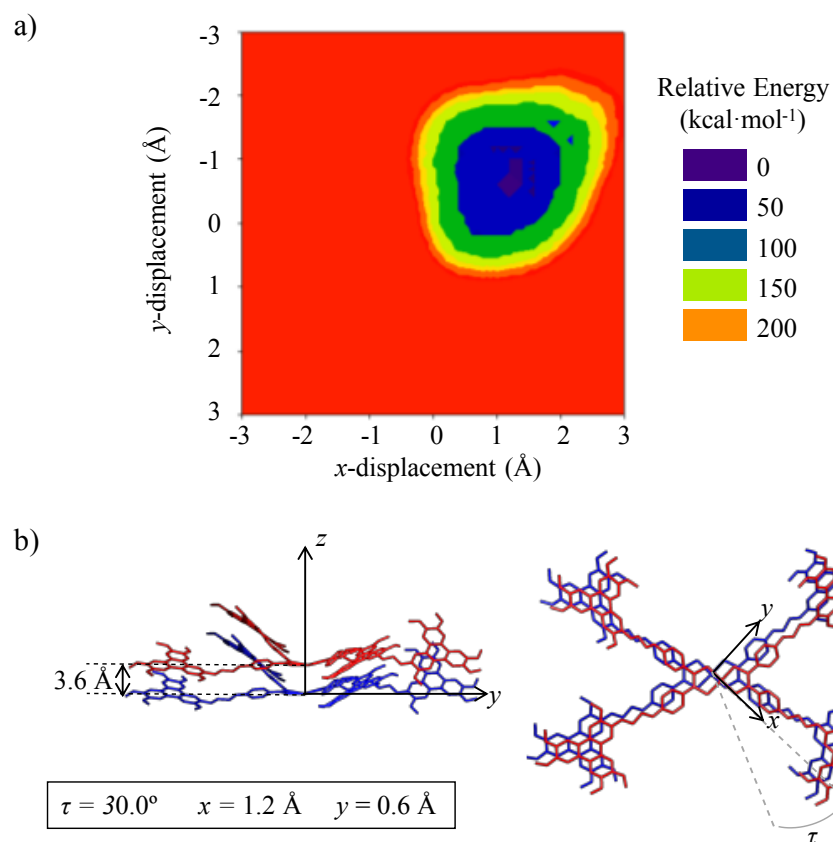
Figure S62. a) Relative energy evolution of a two-molecule cluster as a function of the azimuthal angle ($\tau = 30.0°$) and the relative x and y displacements (steep = 0.2 Å). Only those situations with energy lower than 200kcal·mol^{-1} are displayed. b) Representation of stacked molecules showing the azimuthal angle ($\tau = 30.0°$) and the x (1.2 Å) and y x (10.6 Å) displacements directions. Molecules stacked along z-axis are in blue and red. Hydrogen atoms are omitted This representation corresponds to the minimum relative energy value.
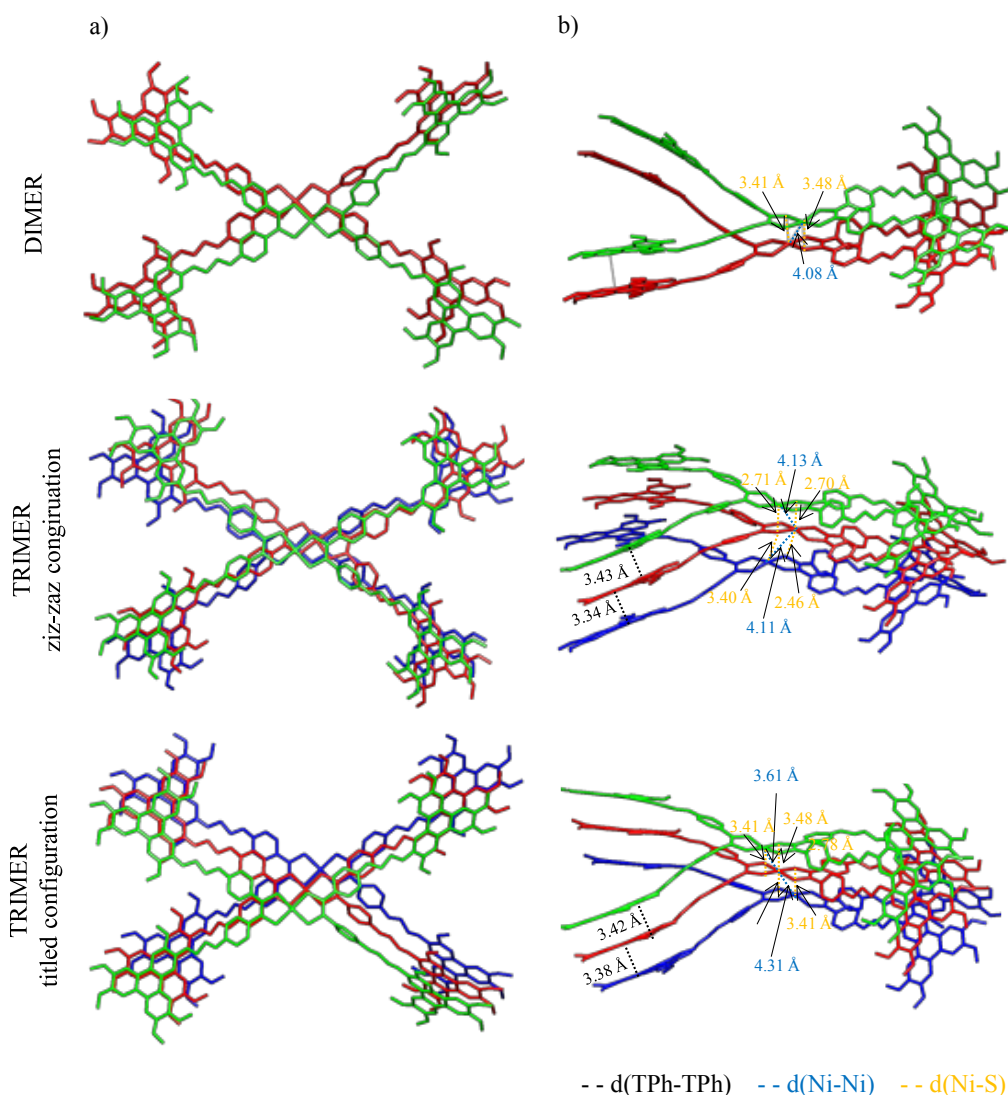
Figure S63. Upper (a) and side (b) views of the minimum-energy structure calculated at the GFN2-xTB level for a dimer and trimer (both ziz-zag and titled configurations) of **4**, along with main intermolecular structural parameters. Each molecule is displayed in a different color, while hydrogen atoms are omitted.

Electronic absorption properties in the mesophase. Vertical transition energies in the mesophase were studied through an ONIOM embedding model over the above optimized tetramer supramolecular cluster. In this model, the two central molecules of the optimized tetramer were treated at TD-CAM-B3LYP-D3BJ/6-31+G(d,p)/Def2-TVZP (high level), while other two surrounding molecules were treated using the GFN2-xTB method (low level). The embedding model enables polarization of the wavefunction of the model system through electrostatic interactions between high and low levels.[18] Similar protocols based on the ONIOM approach along to an electrostatic embedding model have shown to be suitable for studying the structural and

electronic features of dyes in complex environments.[19] Our results highlight that electronic absorption in the NIR region predominantly arises from an intramolecular process. Furthermore, the inclusion of more than one molecule (to account for intermolecular interactions between organometallic fragments) is adequate for an accurate description of the NIR absorption features. In agreement with experimental data (see Figure S32), there is a transition in the NIR region with ΔE_{TD} = 879 nm, which is attributed to a HOMO → LUMO one-electronic transition (with a 96% contribution), with both orbitals located over the Ni-bis(dithiolene) core.
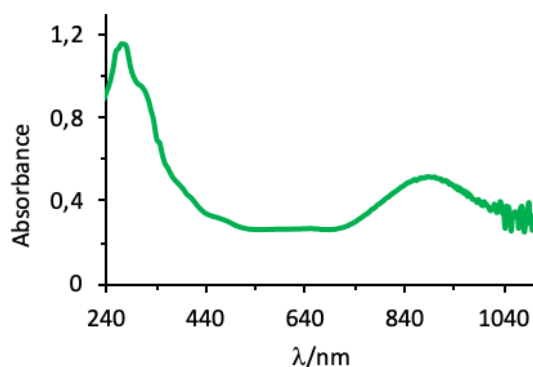
Figure S64. UV-Visible spectra of **4** obtained from a thin film of the supercooled mesophase at room temperature (NIR region, λ_{max} = 884 nm).

References

[1] E. Tritto, R. Chico, G. Sanz-Enguita, C. L. Folcia, J. Ortega, S. Coco, P. Espinet, *Inorg. Chem.,* 2014, **53**, 3449.

[2] C. L. Folcia, I. Alonso, J. Ortega, J. Etxebarria, I. Pintre, M. B. Ros, *Chem. Mater.,* 2006, **18**, 4617.

[3] a) J. M. Granadino-Roldán, A. Garzón, G. García, M. Moral, A. Navarro, M. P. Fernández-Liencres, T. Peña-Ruiz, M. Fernández-Gómez, *J. Phys. Chem. C,* 2011, **115**, 2865; b) C. Maeda, T. Shirakawa, T. Ema, *Chem. Comm.,* 2020, **56**, 15048.

[4] C. Bannwarth, S. Ehlert, S. Grimme, *J. Chem. Theory Comput.,* 2019, **15**, 1652.

[5] A. S. Christensen, T. Kubař, Q. Cui, M. Elstner. *Chem. Rev.,* 2016, **116**, 5301.

[6] M. Bursch, H. Neugebauer, S. Grimme, *Angew. Chem. Int. Ed.,* **2019**, 58, 11078.

[7] C. Bannwarth, E. Caldeweyher, S. Ehlert, A. Hansen, P. Pracht, J. Seibert, S. Spicher, S. Grimme, *WIREs Comput. Mol. Sci.,* 2021, **11**, e1493.

[8] F. Neese, *WIREs Comput. Mol. Sci.,* 2012, **2**, 73.

[9] A. Chantzis, A. D. Laurent, C. Adamo, D. Jacquemin, *J. Chem. Theory. Comput.,* 2013, **9**, 4517.

[10] a) S. Grimme, S., *J. Chem. Phys.,* 2013, **138**, 244104; b) T. Risthaus, A. Hansen, S. Grimme, *Phys. Chem. Chem. Phys.,* 2014, **16**, 14408.

[11] S. Grimme, S. Ehrlich, L. Goerigk, *J. Chem. Theory. Comput.,* 2011, **32**, 1456.

[12] C. Adamo, D. Jacquemin, *Chem. Soc. Rev.,* 2013, **42**, 845.

13 S. Ehlert, M. Stahn, S. Spicher, S. Grimme, *J. Chem. Theory Comput.,* 2021, **17**, 4250.

14 V. Barone, M. Cossi, *J. Phys. Chem. A,* 1998, **102**, 1995.

15 E. R. Johnson, S. Keinan, P. Mori-Sánchez, J. Contreras-García, A. J. Cohen, W. Yang, *J. Am. Chem. Soc.,* 2010, **132**, 6498.

16 T. Lu, F. Chen, *J. Comput. Chem.,* 2012, **33**, 580.

17 a) VMD. http://www.ks.uiuc.edu/Research/vmd/; b) W. Humphrey, A. Dalke, K. Schulten, *J. Mol. Graph.,* 1996, **14**, 33.

18 L. W. Chung, W. M. C. Sameera, R. Ramozzi, A. J. Page, M. Hatanaka, G. P. Petrova, T. V. Harris, X. Li, Z. Ke, F. Liu, H.-B. Li, L. Ding, K. Morokuma, *Chem. Rev.,* 2015, **115** , 5678.

19 a) D. Presti, F. Labat, A. Pedone, M. J. Frisch, H. P. Hratchian, I. Ciofini, M. C. Menziani, C. Adamo, *J. Chem. Theory Comput.,* 2014, **10**, 5577; b) G. García, I. Ciofini, M. Fernández-Gómez, C. Adamo, *J. Chem. Phys. Lett.,* 2013, **4**, 1239; c) S. Del Galdo, B. Chandramouli, G. Mancini, V. Barone, *J. Chem. Theory Comput.,* 2019, **15**, 3170; d) A. Navarro, S. B. Jiménez-Pulido, A. Garzón-Ruiz, N. A. Illán-Cabeza, F. Hueso-Ureña, A. Alejo-Armijo, M. N. Moreno-Carretero, *Dyes Pigm.,* 2019, **168**, 281; e) F. de Lera-Garrido, R. Domínguez, M. P. Fernández-Liencres, C. Martín, J. Tolosa, E. M. García-Frutos, J. Perles, J. Hofkens, J. C. García-Martínez, A. Garzón-Ruiz, A. Navarro, *Dyes Pigm.*, 2023, **213**, 111179.